



**HAL**  
open science

# Unveiling structural defects by $^{139}\text{La}$ NMR and Raman spectroscopies at the origin of surface stability for the design of cerium-based catalysts

Rémy Pointecouteau, Pierre Florian, Vincent Rodriguez, Nicolas Bion, Alain Demourgues

## ► To cite this version:

Rémy Pointecouteau, Pierre Florian, Vincent Rodriguez, Nicolas Bion, Alain Demourgues. Unveiling structural defects by  $^{139}\text{La}$  NMR and Raman spectroscopies at the origin of surface stability for the design of cerium-based catalysts. *Journal of Physical Chemistry C*, 2023, 127 (6), pp.3020-3031. 10.1021/acs.jpcc.2c07034 . hal-04012939

**HAL Id: hal-04012939**

**<https://hal.science/hal-04012939v1>**

Submitted on 3 Mar 2023

**HAL** is a multi-disciplinary open access archive for the deposit and dissemination of scientific research documents, whether they are published or not. The documents may come from teaching and research institutions in France or abroad, or from public or private research centers.

L'archive ouverte pluridisciplinaire **HAL**, est destinée au dépôt et à la diffusion de documents scientifiques de niveau recherche, publiés ou non, émanant des établissements d'enseignement et de recherche français ou étrangers, des laboratoires publics ou privés.

# Unveiling Structural Defects by $^{139}\text{La}$ NMR and Raman Spectroscopies at the Origin of Surface Stability for the Design of Cerium-Based Catalyst

Rémy Pointecouteau<sup>1,2</sup>, Pierre Florian<sup>3</sup>, Vincent Rodriguez<sup>4</sup>, Nicolas Bion<sup>2</sup> and Alain Demourgues<sup>1\*</sup>

1. CNRS, University of Bordeaux, Bordeaux INP, ICMCB UMR CNRS 5026, F-33600, Pessac, France

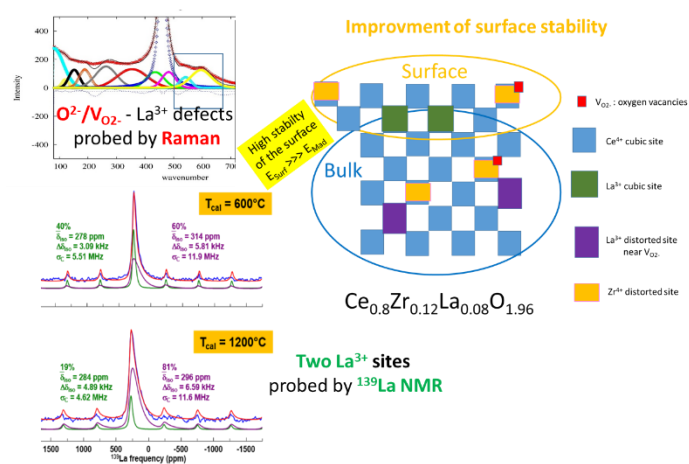
2. Institut de Chimie des Milieux et Matériaux de Poitiers (IC2MP), University of Poitiers, CNRS UMR 7285, TSA51106 – F86073 Poitiers Cedex 9, France.

3. CNRS, UPR CNRS 3079 CEMHTI, F-45100, Orléans, France

4. Institut des Sciences Moléculaires, UMR 5255 CNRS, Université de Bordeaux, 351 Cours de la Libération, F-33405 Talence Cedex, France

**KEYWORDS:** ceria based materials, surface area, structural defects,  $^{139}\text{La}$  solid state NMR, Raman spectroscopy.

**ABSTRACT:** Cerium-based complex oxides are essential materials well suited for numerous applications related to heterogeneous catalysis and electrocatalysis. However, the impact of structural defects on the thermal stability of the surface has still to be elucidated. Probing lanthanum environments by  $^{139}\text{La}$ -NMR and analyzing for the first time in parallel the associated defects by Raman spectroscopy allow for a better view of the structural defects at the surface and in the bulk for samples annealed at  $T=600^\circ\text{C}$  and  $T=1200^\circ\text{C}$ , respectively. Moreover, we propose another indexing of the Raman spectra of cerium-based compounds with fluorite structure by considering two tetrahedral environments around the cationic defects. We evidence the existence of an unusual isolated La pseudo-cubic site, in a series of cerium, zirconium and lanthanum-based oxides. It is found to be stabilized at the subsurface farther from surface's Zr atoms and oxygen vacancies.  $\text{La}^{3+}$  ions in the bulk are preferentially associated to bulk  $\text{Zr}^{4+}$  cations as in  $\text{La}_2\text{Zr}_2\text{O}_7$  ternary compound. When this peculiar  $\text{La}^{3+}$  environment surrounding exclusively by  $\text{Ce}^{4+}$  cubic sites is thermally stable, the specific surface area remains interesting for catalytic application at high temperature. However, enhancing the La and Zr contents tends to increase the association of  $\text{La}^{3+}$  and  $\text{Zr}^{4+}$  ions in clusters and induce a loss of surface area.



## INTRODUCTION

Cerium-based oxides have been widely described in the literature<sup>1-4</sup> and used as automotive exhaust catalysts<sup>5-7</sup> and electrolytes in solid oxide fuel cells<sup>8</sup>. In these applications, the reducibility of Ce<sup>4+</sup> at low temperatures, creating oxygen vacancies into ceria CeO<sub>2-x</sub>, further noted V<sub>O2-</sub>, is a key feature<sup>9,10</sup>. The oxygen storage capacity (OSC) and the oxygen mobility are strongly connected to specific local environments of cerium, zirconium and oxygen in the fluorite-type network. In ceria-zirconia solid solution, the equimolar composition Ce<sub>0.5</sub>Zr<sub>0.5</sub>O<sub>2</sub> exhibits the best oxygen mobility and OSC<sup>11</sup>. The presence of zirconia increases the reducibility at low temperature by modifying the Ce<sup>4+</sup> local environment and increases the ionicity of the Ce<sup>4+</sup>-O<sup>2-</sup> chemical bonding. On the basis of inductive effect, covalent Zr<sup>4+</sup>-O<sup>2-</sup> bond contributes to generate more ionic Ce<sup>4+</sup>-O<sup>2-</sup> bond and consequently more Ce<sup>3+</sup> sites under reducing atmosphere<sup>9,12,13</sup>. The La/Y codoping into ceria improves the ionic conductivity at high temperatures<sup>14-16</sup> by introducing V<sub>O2-</sub>. The trivalent rare earths (La, Y) used in Three Way Catalysts are often necessary to improve thermal stability by keeping sufficient surface area at high temperatures and by promoting ceria support and noble metal interactions<sup>4,17-19</sup>. With respect to the catalytic activity, the synergy between rare earths and oxygen atoms in these highly complex systems remains unclear. In order to shed light on these peculiar effects, the key role of structural features associating local and extended defects must be clearly analyzed by choosing target compositions.

On a structural point of view, oxygen atoms tetrahedrally coordinated to rare earths in cubic symmetry are inter-connected in two sub-networks<sup>7,20</sup>. The redox capacity of Ce<sup>4+</sup> is strongly related to the ionic character of the Ce<sup>4+</sup>-O<sup>2-</sup> chemical bond as well as the polarizability of O<sup>2-</sup> but also of smaller trivalent rare earths in the vicinity of Ce<sup>4+</sup> ions<sup>13</sup>. Moreover, V<sub>O2-</sub> surrounding trivalent rare earth, tetravalent zirconium or cerium increases the cation polarizability. Based on the fcc lattice of ceria network, various kind of defects can be indeed created and identified but the smallest defect in size is associated to oxygen in the T<sub>d</sub> site. Raman spectroscopy is a powerful tool to explore oxygen vibration mode and hence its associated defects. In the fluorite network of no-defect ceria (space group: Fm-3m, O<sub>h</sub><sup>5</sup>), there are two triply degenerated optical modes at the  $\Gamma$  point of the Brillouin zone (k=0), one infrared (IR) active F<sub>1u</sub> mode and one Raman active mode F<sub>2g</sub>. The LO and the TO modes of the polar IR active mode F<sub>1u</sub> are respectively at 270 cm<sup>-1</sup> and 595 cm<sup>-1</sup><sup>21</sup>. The F<sub>2g</sub> mode at 465 cm<sup>-1</sup> is the symmetric breathing mode of the cubic anionic cage involving only motion of the O atoms<sup>22</sup>, so that its frequency is nearly independent of the mass of the cation located at the center of the body-centered cubic (bcc) structure (with cell origin at (1/2, 0, 0)). The central cation is on an O<sub>h</sub> (centrosymmetric) site where the O atoms are located at each corner (T<sub>d</sub> apolar site) of that cubic elementary structural unit (ESU). There are numerous results in the literature related to Raman peak attribution in ceria-related compounds, associated to O<sub>h</sub>/T<sub>d</sub> oxygen local defects in the fluorite

structure<sup>23-25</sup>. The Raman band intensity, frequency and line shape are often correlated to the catalytic activity and reducibility<sup>26-34</sup>. In this paper, we will focus on that cubic ESU, necessary to analyze the complex defect-induced Raman spectra and to reveal the nature and quantity of such defects into the fluorite network.

In order to identify where V<sub>O2-</sub> are preferentially coordinated in La/Y co-doped ceria-zirconia, <sup>89</sup>Y and <sup>139</sup>La NMR spectroscopies are powerful local probes. Maekawa *et al.*<sup>35</sup>, on the basis of the <sup>89</sup>Y NMR investigation, in the (Ce<sub>x</sub>Zr<sub>1-x</sub>O<sub>2</sub>)<sub>0.8</sub>(YO<sub>1.5</sub>)<sub>0.2</sub> series annealed at 1500°C under air, shows that for Zr-rich phases, V<sub>O2-</sub> are located in the vicinity of Zr/Ce atoms. However, for Ce-rich compositions, V<sub>O2-</sub> appear around Y<sup>3+</sup> ions, confirming that they can have various locations depending on the chemical composition. Moreover, the bulk ionic conductivity which originates from hopping phenomena involving oxygen atoms and vacancies, strongly depends on Zr content with a minimum of conductivity at x=0.5 when V<sub>O2-</sub> are equally distributed between (Ce/Zr) and Y atoms. Furthermore, the bulk ionic conductivity of trivalent rare-earth (RE) doped-ceria is maximum for 5% mol of La<sup>3+</sup> and 10% mol of Gd<sup>3+</sup><sup>36</sup>. EXAFS investigation of Y<sup>3+</sup>/Gd<sup>3+</sup>/La<sup>3+</sup> (10%, 20% and 30%) substituted-ceria annealed at 1600°C, showed that La<sup>3+</sup> and Y<sup>3+</sup> cations form clusters stabilized with V<sub>O2-</sub> whereas Gd<sup>3+</sup> ions remain randomly distributed into the ceria lattice<sup>37</sup>. However, this statement is controversial and depends mainly on the RE content. By Pair Distribution Function (PDF) analysis, of Ce<sub>1-x</sub>Gd<sub>x</sub>O<sub>2-x/2</sub> complex oxides with x ≥ 0.125, a biphasic model with CeO<sub>2</sub>-Fluorite and Gd<sub>2</sub>O<sub>3</sub>-Bixbyite or C-type appears locally between 2 Å and 6 Å<sup>38</sup>. Moreover, PDF analysis, of Ce<sub>0.75</sub>La<sub>0.25</sub>O<sub>1.875</sub> complex oxide, revealed also a fraction of C-type phase with short-range order<sup>39</sup>. Furthermore <sup>89</sup>Y and <sup>17</sup>O MAS-NMR analysis of Ce<sub>1-x</sub>Y<sub>x</sub>O<sub>2-x/2</sub> complex oxides with 0.05 ≤ x ≤ 0.30, showed the occurrence of few Y-Y interactions for low Y content with, for instance, calculated populations Ce<sub>2</sub>Y<sub>2</sub> around oxygens at 1% for x = 0.05 and 5 % for x=0.10<sup>40</sup>. So, the formation of RE-RE clusters into the ceria network is strongly dependent on the nature of the RE element, its concentration and the final composition with other dopants such as Zr<sup>4+</sup>. A question is opened: is there a relationship between the random distribution of RE in the ceria lattice or the occurrence of RE-RE interactions and clusters, which limits the bulk ionic conductivity? Previous studies on Ce<sub>2</sub>Sn<sub>2</sub>O<sub>7</sub>-Ce<sub>2</sub>Sn<sub>2</sub>O<sub>8</sub> pyrochlore solid solution based on in-situ neutron diffraction and <sup>119</sup>Sn NMR, allow for the identification of the complex organization of metals and oxygens during the redox process<sup>41</sup>. More recently, in Ce<sub>1-x</sub>Fe<sub>x</sub>O<sub>2-x/2</sub> solid solutions with various morphologies, by in situ XANES-EXAFS experiments, Mossbauer and ESR spectroscopies<sup>42,43</sup>. Fe valence states and clusters have been identified and also play key roles in the reducibility properties. Very recently, by exploring the complex phase diagram CeO<sub>2</sub>-ZrO<sub>2</sub>-PrO<sub>x</sub>, we outlined the impact of Pr valence state on oxygen mobility, redox and transport properties of these complex oxides<sup>44</sup>.

Various coordinations can be found for the cations: Ce<sup>4+</sup> has a strong affinity to occupy a cubic site in pure ceria, the smaller Zr<sup>4+</sup> is typically 7-fold coordinated in ZrO<sub>2</sub> and Y<sup>3+</sup> is located

in a prism and an octahedron in  $Y_2O_3$ . Thus, the preferential location of  $V_{O2-}$  around  $Y^{3+}$  in Ce-rich phases has a tendency to stabilize  $Ce^{4+}$  in 8-fold and  $Y^{3+}$  ions mainly in 7-fold coordination. In Yttrium-stabilized Zirconia,  $V_{O2-}$  are mainly located on  $Zr^{4+}$  cations, leaving  $Y^{3+}$  in a more or less cubic symmetry<sup>35</sup>. However, the situation with larger  $La^{3+}$  ions is unclear: taking into account that  $La^{3+}$  exhibits the highest polarizability in the rare earth series, should it be located in a larger site? Furthermore, no information exists on complex oxides annealed at temperatures low enough to maintain high surface area and catalytic activity. It is then relevant to follow the thermal history of the complex oxides.

Raman spectroscopy allows to explore variation of the electron density, especially in the vicinity of oxygen giving valuable information on defects in the ceria lattice.  $^{139}La$  NMR probes on the other hand the local geometry around lanthanum such as coordination number, La-O bond distance and O-La-O bond angle variations. By combining Raman and  $^{139}La$  NMR spectroscopies, we can then clearly evidence the interactions between oxygen defects and trivalent rare-earths. For the targeted  $Ce_{1-x-y}Zr_xLa_yO_{2.8}$  compositions of the present study, a La content around 10 at%, with or without Zr atoms, will be firstly considered in order to limit the  $V_{O2-}$  content. This low  $La^{3+}$  content mimics the 8 at% of  $Y^{3+}$  found in Yttrium-stabilized Zirconia, the best ionic conductor. Other compositions with larger (Zr+La) loadings and a La/Zr atomic ratio always equal to 1 will also be investigated. As a first approximation, the expected behavior is that the ionic volume taken by  $La^{3+}$ , the large polarizable cation, will be compensated by that of  $Zr^{4+}$ , the smaller polarizing cation. This is observed in  $La_2Zr_2O_7$  pyrochlore related to fluorite-type structure where large  $La^{3+}$  scalenohedral [2+6] sites are associated with the smaller  $Zr^{4+}$  ions stabilized in an octahedral environment<sup>45</sup>. Two annealing temperatures under air, 600°C and 1200°C will be considered. A discussion will be engaged in order to reveal the impact of La local environment and associated defects on the thermal stability of the surface.

## EXPERIMENTAL SECTION

### Sample preparation

The rare earth-based mixed oxides  $Ce_{1-x-y}Zr_xLa_yO_2$   $0.1 \leq x+y \leq 0.4$  were synthesized by co-precipitation in basic medium at room temperature followed by annealing under air at different temperatures. The various precursors were nitrate solutions from SOLVAY, including cerium nitrate (99.9% and  $[Ce] = 2.92$  mol/L), zirconium nitrate (99.9% and  $[Zr] = 1.60$  mol/L), and lanthanum nitrate (99.9%,  $[La] = 2.85$  mol/L). In each case, stoichiometric amounts of salts to reach the targeted compositions were mixed and adjusted with water to get 50 mL of solution. The nitrate solution was added dropwise into a mixture of 150 mL of diluted ammonia (M/100) and 35 mL of concentrated ammonia (35%) while a steady pH = 10 is maintained during the precipitation step and the maturation under air which lasted 4h. The solution was centrifuged 4 times successively with a diluted ammonia solution (M/1000) and 2 times with absolute ethanol. The solid was dried on a sand bath at 50°C overnight and then annealed at 600°C or 1200°C for 12h under air.

The chemical compositions of the targeted sample were confirmed by Inductively Coupled Plasma analysis (Table 1-SI).

### XRD analysis

Powder X-ray diffraction patterns were recorded on a PANalytical X'Pert MPD apparatus equipped with a  $Cu K\alpha_1/K\alpha_2$  radiation ( $\lambda_1=1.5406$  Å,  $\lambda_2=1.5442$  Å) and an X'Celerator detector. Data were collected over a range of 10°-80° with 0.017° steps. The lattice parameters and the crystallite sizes were determined by profile matching (Le-Bail fit) using the Thomson-Cox-Hastings function with the JANA2006 program package.

### BET analysis

$N_2$  physisorption experiments were conducted with a Tristar 3000 (Micromeritics). In each case, the sample was firstly outgassed 2h under vacuum at 250 °C.  $N_2$  adsorption was then performed at -196 °C and the specific surface areas were determined from the Brunauer-Emmett-Teller (BET) method in the 0.05–0.25 P/P<sub>0</sub> relative pressure range.

### Raman spectroscopy

Raman spectra were recorded at room temperature on a Xplora confocal Raman microscope from Horiba Scientific (objective 50×, NA=0.50), using a CW 532 nm laser excitation. The laser power was less than 15 mW for all samples. The spectrometer includes a grating with 1800 grooves/mm and an air-cooled CCD. Unpolarised Raman spectra were measured over the frequency range 50–1500  $cm^{-1}$  with a spectral resolution better than 3  $cm^{-1}$ . The deconvolution of the Raman spectra was simultaneously obtained using the same (as much as possible) weighted Gaussian/Lorentzian (pseudo-Voigt) profile for the materials considered. The defect-induced Raman bands had in most cases a Gaussian profile (>90%) whereas the Raman-active  $F_{2g}$  band from ceria *ca* 465 $cm^{-1}$  had nearly a 100% Lorentzian profile which is consistent for a periodic lattice phonon band (even when defects are present). For a given band profile, the full width at half maximum (FWHM) and energy positions were slightly modifiable during deconvolution (in the range of 0–2%) but were constrained to be similar for all spectra to maintain a continuous consistency between compounds. Particular attention was paid to adjusting as well as possible the different bands of spectra, but always with a minimum number of bands as expected in regards to the considered polyhedral ESU detailed in the Raman study section. Note that only the high frequency range including the  $F_{2g}$  Raman active band of pure ceria were exploited for quantitative purpose and compared to the NMR results. Finally, since the only allowed phonon band is the ceria Raman-active  $F_{2g}$  band, fitted intensities were normalized to that band for each complex oxides in order to get a valuable reference between all of them. Note that another possibility could be to normalize the fitted intensities to the total spectral density of each spectrum. We did not choose this method since we think that the total spectral density is too much sensible to the lower spectral range (see for example figure 2c), and

therefore may not be enough correlated with the real defect contributions, evidenced in the higher frequency part of each Raman spectrum.

### <sup>139</sup>La NMR study

All experiments were performed at 20.0 T on a Bruker Avance Neo spectrometer operating at a Larmor frequency of 120.1 MHz, and are referenced to a 1M solution of LaCl<sub>3</sub>.

Static experiments were performed in a 4mm probe (~300 mg of sample) using a Hahn echo sequence, an echo delay of 8.5 μs, 20 kHz radio-frequency field and short pulse durations of 1 μs and 2 μs (i.e. less than 90°/180° pulses). With these conditions, we ensure that the full spectrum width is excited. A recycle delay of 0.25 s was sufficient to optimize the signal-to-noise ratio and typically 24000 scans were accumulated (i.e. ~2h).

Magic angle spinning experiments were performed with a 1.3 mm probe (~10 mg of sample) spinning at 62 kHz. Spectra were recorded with a Hahn echo sequence using an echo delay of 1 rotor period, a radio-frequency field of 100 kHz and pulse durations of 0.625 μ and 1.25 μs (corresponding to the transition selective 90° and 180° pulses). A recycle delay of 0.25 s was used and typically 300000 scans were accumulated (i.e. ~24h).

Simulations were performed using the “Czjzek”<sup>46</sup> also called “Gaussian Isotropic Model” (GIM) model implemented in DMFit<sup>47, 48</sup>. In DMFit this model, based solely on the Central Limit Theorem and on statistical isotropy, contains four adjustable parameters: the line intensity, the position (average isotropic chemical shift  $\bar{\delta}_{iso}$ ), its distribution  $\Delta\bar{\delta}_{iso}$  and the mode of the quadrupolar coupling distribution  $C_{Q,mode}$  directly linked to the width  $\sigma_C$  of this distribution through  $\sigma_C = C_{Q,mode}/2$  (see discussion part for further description). To better constrain the fit, the later was performed simultaneously on both the static and the MAS spectra. Whenever possible, the spinning sidebands of the satellite transition were also taken into account.

## RESULTS AND DISCUSSION

X-Ray diffractograms, depicted in Figures 1-2 SI for complex oxides annealed at T=600°C and T=1200°C reveal pure phases, except for Ce<sub>0.8</sub>Zr<sub>0.2</sub>O<sub>2</sub> and Ce<sub>0.62</sub>Zr<sub>0.3</sub>La<sub>0.08</sub>O<sub>1.96</sub> oxides calcined at T=1200°C (Fig 2-SI) where a slight phase separation is observed.

The refined unit-cell parameter of the fluorite network and the crystallite size are reported in Tables 1 and 1-SI. The specific surface areas of Ce<sub>0.8</sub>Zr<sub>0.2</sub>O<sub>2</sub> and Ce<sub>0.8</sub>Zr<sub>0.12</sub>La<sub>0.08</sub>O<sub>1.96</sub>, Ce<sub>0.62</sub>Zr<sub>0.3</sub>La<sub>0.08</sub>O<sub>1.96</sub> determined by BET method on samples annealed at T = 600°C, 1000°C and 1200°C are also mentioned.

Table 1 : Structural and textural characteristics of Ce<sub>1-x-y</sub>Zr<sub>x</sub>La<sub>y</sub>O<sub>2-y/2</sub> oxides annealed under air

Compositions	Cell Parameters	Crystallite size (nm)	Surface area	Surface area	Surface area
	(Å) (Tcal = 600°C)		(m <sup>2</sup> /g) (Tcal = 600°C)	(m <sup>2</sup> /g) (Tcal = 1000°C)	(m <sup>2</sup> /g) (Tcal = 1200°C)
Ce <sub>0.9</sub> La <sub>0.1</sub> O <sub>1.95</sub>	5.442 (1)	13 (1)	44	<1	<1
Ce <sub>0.8</sub> Zr <sub>0.2</sub> O <sub>2</sub>	5.394 (2)	10 (1)	50	<1	<1
Ce <sub>0.8</sub> Zr <sub>0.12</sub> La <sub>0.08</sub> O <sub>1.96</sub>	5.426 (2)	7 (1)	86	23	10
Ce <sub>0.7</sub> Zr <sub>0.15</sub> La <sub>0.15</sub> O <sub>1.92</sub>	5.435 (2)	8 (1)	27	<1	<1
Ce <sub>0.6</sub> Zr <sub>0.2</sub> La <sub>0.2</sub> O <sub>1.90</sub>	5.451 (2)	6 (1)	7	<1	<1
Ce <sub>0.62</sub> Zr <sub>0.3</sub> La <sub>0.08</sub> O <sub>1.96</sub>	5.403 (3)	9 (1)	54	<1	<1

For a fixed Zr amount, the higher the La content, the higher the unit cell parameter in good agreement with the larger ionic size of La<sup>3+</sup> with respect to Zr<sup>4+</sup> ions. This also explains the large variation of the unit cell parameter in this series. It is worth noting the high surface area of Ce<sub>0.8</sub>Zr<sub>0.12</sub>La<sub>0.08</sub>O<sub>1.96</sub> complex oxide (S<sub>BET</sub> = 86 m<sup>2</sup>/g) as well as the high thermal stability of this sample revealed by a surface area of 10 m<sup>2</sup>/g and a low crystallite size after annealing at 1200°C. For the other compounds, the crystallite size after annealing at 1200°C remains higher (Table 2-SI) consistent with a loss of surface areas. Only Ce<sub>0.8</sub>Zr<sub>0.2</sub>O<sub>2</sub> and Ce<sub>0.62</sub>Zr<sub>0.3</sub>La<sub>0.08</sub>O<sub>1.96</sub> show a phase separation

after annealing at high temperatures (1200°C). The associated tetragonal Zr-rich phase is denoted by an asterisk on the XRD patterns (Fig 2 SI)

### <sup>139</sup>La NMR investigation

Table 2 : Experimental <sup>139</sup>La NMR parameters for reference oxides and La local environment.

Compositions	$\delta_{iso}$ (ppm)	$C_Q$ (MHz)	Coordination number	Bond Length La-O (Å)	References
LaPO <sub>4</sub>	36	47	[9]	2 x 2,47 2,50 2 x 2,54 2,60 2,61 2,67 2,76	(49)
LaBO <sub>3</sub>	230	23	[9]	2,44 2 x 2,46 2 x 2,58 2 x 2,67 2 x 2,77	(51)
La(OH) <sub>3</sub>	260	22	[9]	3 x 2,59 6 x 2,63	(52)
LaNbO <sub>4</sub>	295	36	[8]	2 x 2,47 2 x 2,49 2 x 2,52 2 x 2,54	(52)
La <sub>2</sub> Zr <sub>2</sub> O <sub>7</sub>	410	86	[8]	2 x 2,34 6 x 2,64	This work
La <sub>2</sub> O <sub>3</sub>	620	59	[7]	3 x 2,36 2,46 3 x 2,73	(51)

<sup>139</sup>La is a spin  $I = 7/2$  quadrupolar nucleus with an almost complete natural abundance (99,9%), a moderate gyromagnetic ratio  $g$  ( $\gamma = 3.801 \cdot 10^7 \text{ rad T}^{-1} \text{ s}^{-1}$ ) but a large quadrupolar moment making it very sensitive to the Electric Field Gradient (EFG) generated by surrounding charges. The latter leads to a severe broadening of the line even at high principal magnetic fields and high spinning speeds. The extent of the EFG (i.e. the quadrupolar coupling constant  $C_Q$ ) and its deviation from the cylindrical symmetry (i.e. the symmetry parameter  $\eta_Q$ )<sup>49,50</sup> are usually retrieved from a simulation of the NMR line, along with the isotropic chemical shift  $\delta_{iso}$ . Experimental  $\delta_{iso}$ , and  $C_Q$  <sup>139</sup>La NMR parameters of various oxides and hydroxides are reported in Table 2, illustrating the influence of the local geometry on those parameters. 2.5 at % of La<sup>3+</sup> into CeO<sub>2</sub> leads to a sharp singlet at  $\delta_{iso} = 280 \text{ ppm}$ <sup>51</sup>, confirming that La<sup>3+</sup> cations occupy the cubic site of the fluorite lattice. In La<sub>2</sub>O<sub>3</sub>, La<sup>3+</sup> occupy highly distorted monocapped octahedra with 3 shorter La-O bond lengths at 2.36 Å and  $\delta_{iso}$  increases to 620 ppm as well as the quadrupolar coupling constant which reaches  $C_Q = 59 \text{ MHz}$ , showing the deviation from cubic symmetry. In La(OH)<sub>3</sub>, La<sup>3+</sup> are 9-fold coordinated to oxygen with 3 shorter La-O bond distances at 2.59 Å and the local environment remains closer to the spherical one's with lower  $\delta_{iso} = 260 \text{ ppm}$  and  $C_Q = 22 \text{ MHz}$  values. The large decrease of  $\delta_{iso}$ , from La<sub>2</sub>O<sub>3</sub> to La(OH)<sub>3</sub> is related to the increase of coordination number and La-O shortest bond

lengths. Moreover one should have to note that the ionic character of La-O chemical bond increases from La<sub>2</sub>O<sub>3</sub> to La(OH)<sub>3</sub> and the  $\delta_{iso}$  chemical shift decreases. Furthermore, in ternary compounds, LaPO<sub>4</sub>, LaBO<sub>3</sub>, LaNbO<sub>4</sub> and La<sub>2</sub>Zr<sub>2</sub>O<sub>7</sub>, the influence of M second neighbors (engaging a stronger M-O covalent bond,  $M = P^{5+} > B^{3+} > Nb^{5+} > Zr^{4+}$ ) on  $\delta_{iso}$  chemical shift is high. Through the inductive effect of M cations, the more covalent the M-O bond, the higher the ionic character of the La-O bond and again the lower  $\delta_{iso}$ . Indeed, the chemical shift drastically changes in increasing order from LaPO<sub>4</sub> ( $\delta_{iso} = 36 \text{ ppm}$ ) < LaBO<sub>3</sub>, ( $\delta_{iso} = 230 \text{ ppm}$ ) < LaNbO<sub>4</sub> ( $\delta_{iso} = 295 \text{ ppm}$ ) < La<sub>2</sub>Zr<sub>2</sub>O<sub>7</sub>, ( $\delta_{iso} = 410 \text{ ppm}$ ). In these two last compounds, the coordination number (CN) is equal to 8 whereas in phosphate or borate, it expands to  $CN = 9$ <sup>50,52,53</sup>. Moreover, the quadrupolar coupling constant raises from 36 MHz in LaNbO<sub>4</sub> to 86 MHz in La<sub>2</sub>Zr<sub>2</sub>O<sub>7</sub> because the site moves away from the spherical symmetry.

Figure 1 displays the experimental <sup>139</sup>La MAS spectra obtained for Ce<sub>0.9</sub>La<sub>0.1</sub>O<sub>1.95</sub> and Ce<sub>0.8</sub>Zr<sub>0.12</sub>La<sub>0.08</sub>O<sub>1.96</sub> annealed at 600°C and 1200°C. The lines span over 500 ppm, but without the characteristic sharp discontinuities one would expect for a well ordered compound. Taking into account our results and those of literature<sup>31</sup>, when the La<sup>3+</sup> content increases from 2% mol<sup>51</sup> to 8% mol into ceria, the cubic environment of La<sup>3+</sup> is altered. On the contrary, one recovers a continuous line raising sharply on the left side and decaying slowly on the right edge reminiscent of a continuous distribution of EFG like the one initially proposed by Czjzek<sup>46</sup> and further developed for NMR by Le Caer *et al.*<sup>54</sup> under the acronym "GIM" (Gaussian Isotropic Model). The main hypothesis behind this model is that the EFG tensor elements are randomly distributed, or in other words that they are sums over a large number of random terms with various physical origins (such as, but not limited to, bond lengths and bond angles). Although this hypothesis could appear awkward in the context of crystalline materials, it makes reasonable sense under the assumption of a random distribution throughout the network of cations onto the unique A lattice site of the fluorite structure, as well as  $V_{O^{2-}}$ . It has indeed early been shown that a non-relaxed cubic solid with a high density of vacancies display a Czjzek-like distribution of EFG<sup>55</sup>. As seen in Figure 1, the Czjzek model does indeed provide a very satisfactory simulation using a one- or two-component fit accounting simultaneously for both the static and the MAS spectra (see supplementary materials). One retrieves then the average (most probable) isotropic chemical shift  $\bar{\delta}_{iso}$  along with the full width at half maximum of its Gaussian distribution  $\Delta\delta_{iso}$ , and a unique quadrupolar parameter  $\sigma_C$ , the width of the distribution (or its variance  $\sigma_C^2$ ) of the elements of the EFG.  $\sigma_C$  measures the extent of the atomic-level disorder present in the sample and has lost any specific structural feature it originates from<sup>56</sup>. An increase in  $\sigma_C$  can be viewed as an increase in "structural disorder", e.g. an increase in the width of the distribution of La-O bond lengths and O-La-O bond angle. <sup>139</sup>La NMR experimental parameters  $\bar{\delta}_{iso}$ ,  $\Delta\delta_{iso}$  and  $\sigma_C$  of all investigated cerium-based oxides are reported in Table 3 and Table 3-SI.

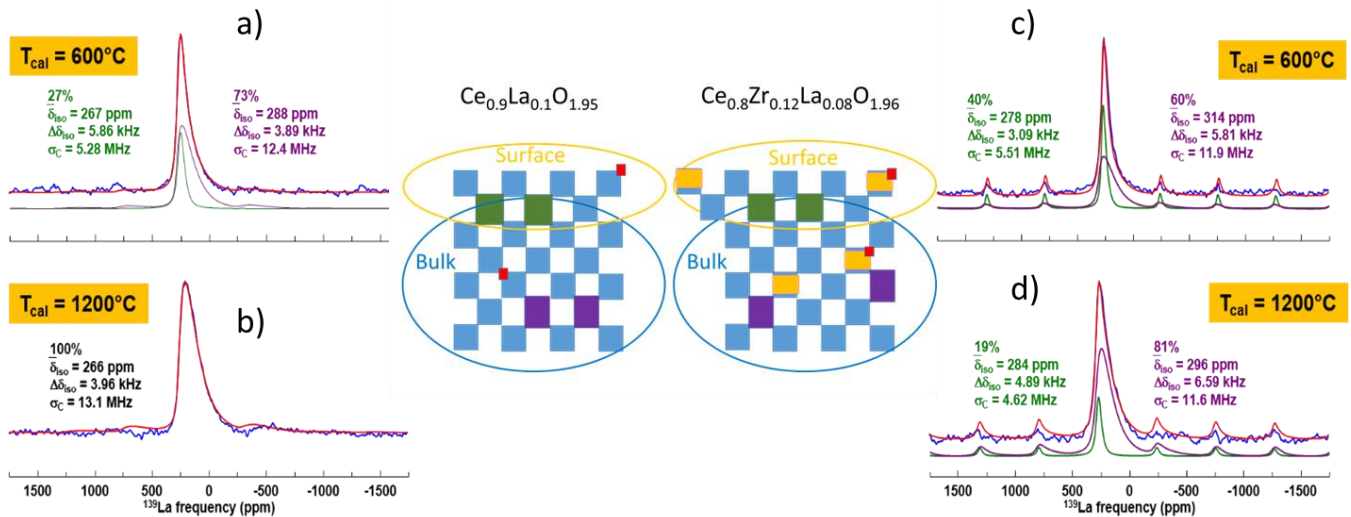


Figure 1:  $^{139}\text{La}$  MAS NMR spectra of  $\text{Ce}_{0.9}\text{La}_{0.1}\text{O}_{1.95}$  (left, a & b) and  $\text{Ce}_{0.8}\text{Zr}_{0.12}\text{La}_{0.08}\text{O}_{1.96}$  (right, c & d) annealed at  $600^\circ\text{C}$  (top a & c) and  $1200^\circ\text{C}$  (bottom, b & d). Line shape simulation are shown in red (sum of site 1 & 2), green (site 1) and violet (site 2). On the basis of the  $^{139}\text{La}$  NMR investigations, schematic representations of the surface-subsurface-bulk network of the  $\text{Ce}_{0.9}\text{La}_{0.1}\text{O}_{1.95}$  and  $\text{Ce}_{0.8}\text{Zr}_{0.12}\text{La}_{0.08}\text{O}_{1.96}$  oxides.  $\text{La}_{\text{Ce}}$  sites (far from oxygen vacancies and Zr atoms) are represented in green,  $\text{La}_{\text{Def}}$  sites in violet,  $\text{Zr}^{4+}$  site in orange, oxygen vacancies  $\text{V}_{\text{O}^{2-}}$  in red and  $\text{Ce}^{4+}$  in blue

For  $\text{Ce}_{0.9}\text{La}_{0.1}\text{O}_{1.95}$  annealed at  $1200^\circ\text{C}$ , the NMR spectrum can be well simulated using a single component with a large distribution (Figure 1 and 5-SI). Its  $\bar{\delta}_{iso}$  is among the lowest at 266 ppm with  $\sigma_C$  around 13.1 MHz, a high value illustrating a structural disorder arising from the presence of many lanthanum configurations. The  $\text{La}^{3+}$  local environment is no more cubic but distorted (non-zero EFG) and the site distribution is disordered. Annealing at  $600^\circ\text{C}$  produces a sharper signal (Figure 1) for which a single component does not allow to account satisfactorily for both the static and the MAS spectra (Figure 3-SI). The first component (27%) is characterized by  $\bar{\delta}_{iso} = 266$  ppm and a  $\sigma_C$  around 5.3 MHz whereas the second (73%) by  $\bar{\delta}_{iso} = 288$  ppm and a significantly bigger  $\sigma_C$  around 12.4 MHz. Both  $\bar{\delta}_{iso}$  indicate that those two sites correspond to 8-fold coordinated  $\text{La}^{3+}$  in accordance with their position on the A site of the fluorite structure. We propose that this difference in local disorder at the La site is linked to the absence/presence of  $\text{V}_{\text{O}^{2-}}$  oxygen vacancies as defects in the nearest neighborhood of those La sites. In the absence of such defects the structural disorder originates from the statistical occupancy of the A sites by either La and Ce with various La-O bond distances. One should underline that the first less disordered environment (27%) should also correspond to the 2% ( $0.27 \times 8\%$ ) of  $\text{La}^{3+}$  detected in cubic environment in the  $\text{Ce}_{0.9}\text{La}_{0.02}\text{O}_{1.99}$  phase<sup>41</sup>. Then, one can assume that this isolated  $\text{La}^{3+}$  site surrounded by 12  $\text{Ce}^{4+}$  as second neighbors in cubic environments must become pseudo-cubic. Additional presence of defects such as  $\text{V}_{\text{O}^{2-}}$  for oxygen

vacancies or  $\text{Zr}^{4+}$  for the following compositions, induces an additional structural variable which increases the extent of the structural disorder and hence  $\sigma_C$ . In the following we will refer to these two lanthanum environments as  $\text{La}_{\text{Ce}}$  (low  $\bar{\delta}_{iso}$  and  $\sigma_C$ ) and  $\text{La}_{\text{Def}}$  (high  $\bar{\delta}_{iso}$  and  $\sigma_C$ ) respectively.

$\text{Ce}_{0.8}\text{Zr}_{0.12}\text{La}_{0.08}\text{O}_{1.96}$  annealed at  $600^\circ\text{C}$  (Fig 1) shows an increased proportion of  $\text{La}_{\text{Ce}}$  site (40%,  $\bar{\delta}_{iso} = 278$  ppm,  $\sigma_C = 5.5$  MHz) (Table 3) while increasing the chemical shift of both these sites due probably to a slight decrease of the La-O bond distances. Compared to  $\text{Ce}_{0.9}\text{La}_{0.1}\text{O}_{1.95}$ , the isotropic chemical shift of  $\text{La}_{\text{Def}}$  ( $\bar{\delta}_{iso} = 314$  ppm,  $\sigma_C = 11.9$  MHz) increases significantly and approaches the 410 ppm value found for  $\text{La}_2\text{Zr}_2\text{O}_7$  (table 2). This increase therefore shows the presence of the ( $\text{V}_{\text{O}^{2-}}$ ,  $\text{Zr}^{4+}$ ) defects in the vicinity of this site while keeping the 8-fold coordination found in  $\text{La}_2\text{Zr}_2\text{O}_7$ . After annealing at  $T = 1200^\circ\text{C}$ , the two sites  $\text{La}_{\text{Ce}}$  and  $\text{La}_{\text{Def}}$  (20%/80%) are still evidenced by their  $\sigma_C$  (resp. 4.6 MHz and 11.6 MHz) but display closer  $\bar{\delta}_{iso}$  (resp. 284 ppm and 296 ppm). Surprisingly, after annealing at  $T=600^\circ\text{C}$ , the presence of  $\text{Zr}^{4+}$  ions, favors again an 8-fold coordination labelled  $\text{La}_{\text{Ce}}$  for  $\text{La}^{3+}$  in pseudo-cubic coordination, mainly surrounded by  $\text{Ce}^{4+}$  as second neighbors and far from ( $\text{V}_{\text{O}^{2-}}$ ,  $\text{Zr}^{4+}$ ) defects. The clear decrease of  $\text{La}_{\text{Def}}$   $\bar{\delta}_{iso}$  upon increasing  $T_{\text{cal}}$  from  $600^\circ\text{C}$  to  $1200^\circ\text{C}$  (resp. 314 ppm to 296 ppm) when the values for  $\text{La}_{\text{Ce}}$  are almost constant (resp. 278 ppm to 284 ppm) shows the influence of ( $\text{V}_{\text{O}^{2-}}$ ,  $\text{Zr}^{4+}$ ) defects in the neighborhood of the former.

Table 3: Experimental  $^{139}\text{La}$  NMR parameters for  $\text{Ce}_{1-x-y}\text{Zr}_x\text{RE}_y\text{O}_{2-z}$  annealed at  $600^\circ\text{C}$  under air. Error bars are given in Table 4-SI.

Compositions ( $T_{\text{cal}} = 600^\circ\text{C}$ )	% site (1)	$\bar{\delta}_{\text{iso}}$ (1) (ppm)	$\Delta\bar{\delta}_{\text{iso}}$ (1) (ppm)	$\sigma_c$ (1) (MHz)	% site (2)	$\bar{\delta}_{\text{iso}}$ (2) (ppm)	$\Delta\bar{\delta}_{\text{iso}}$ (2) (ppm)	$\sigma_c$ (2) (MHz)
$\text{Ce}_{0.9}\text{La}_{0.1}\text{O}_{1.95}$	27	267	48.8	5.28	73	288	34.2	12.1
$\text{Ce}_{0.8}\text{Zr}_{0.12}\text{La}_{0.08}\text{O}_{1.96}$	40	278	25.7	5.51	60	314	48.4	11.9
$\text{Ce}_{0.7}\text{Zr}_{0.15}\text{La}_{0.15}\text{O}_{1.92}$	31	275	70.1	5.55	69	293	29.5	13.8
$\text{Ce}_{0.6}\text{Zr}_{0.2}\text{La}_{0.2}\text{O}_{1.90}$	37	278	38.8	10.1	63	338	54.1	20.1

For  $\text{Ce}_{0.9}\text{La}_{0.1}\text{O}_{1.90}$  and  $\text{Ce}_{0.8}\text{Zr}_{0.12}\text{La}_{0.08}\text{O}_{1.96}$  compositions, the surface area is equal to  $44 \text{ m}^2/\text{g}$  and  $86 \text{ m}^2/\text{g}$  respectively (Table 1). Taking into account the strong ability of  $\text{Zr}^{4+}$  ions to stabilize the surface in ceria-based materials as well as their affinity to be 7-fold coordinated to oxygen, it is reasonable to consider the stabilization of ( $V_{\text{O}_2^-}$  oxygen vacancies happens preferentially at the surface in the vicinity of  $\text{Zr}^{4+}$ . Upon annealing at  $1200^\circ\text{C}$  the surface collapses and the amount of  $\text{La}_{\text{Def}}$  environments increases because ( $V_{\text{O}_2^-}$ ,  $\text{Zr}^{4+}$ ) defects migrate towards the bulk. Thus, large and saturated  $\text{La}_{\text{Ce}}$  sites are mainly found at the sub-surface (below the third atomic layer), far from  $\text{Zr}^{4+}$  ions stabilized with  $V_{\text{O}_2^-}$  oxygen vacancies and found at the surface. It is always hard to make a difference between surface and sub-surface but in order to avoid broken bonds at the surface, it is more reasonable to consider the pseudo-cubic  $\text{La}_{\text{Ce}}$  sites surrounding by cubic  $\text{CeO}_3$  environments at the subsurface. Structural relaxation also takes place at the surface leading to  $\text{La-O}$  bond lengths raising and can hence lead to the formation of  $\text{La}_{\text{Ce}}$  pseudo-cubic environments.

At  $T_{\text{cal}} = 600^\circ\text{C}$ , increasing La and Zr contents while keeping atomic ratio  $\text{La}/\text{Zr}$  equal to 1 ( $\text{Ce}_{0.7}\text{Zr}_{0.15}\text{La}_{0.15}\text{O}_{1.92}$  and  $\text{Ce}_{0.6}\text{Zr}_{0.20}\text{La}_{0.20}\text{O}_{1.90}$  compositions; Figures 7-SI and 8-SI) leads to an increase of the  $\text{La}_{\text{Ce}}$  proportion (resp. 31% and 37%) while keeping  $\bar{\delta}_{\text{iso}}$  constant ( $\sim 277$  ppm). The increase of average isotropic chemical shift  $\bar{\delta}_{\text{iso}}$  of the  $\text{La}_{\text{Def}}$  site with La content in the case of  $\text{Ce}_{0.6}\text{Zr}_{0.20}\text{La}_{0.20}\text{O}_{1.90}$  complex oxide shows an increased presence of Zr in its vicinity (i.e.  $\text{La-O}$  shortest bond distances such as those found in  $\text{La}_2\text{Zr}_2\text{O}_7$ ). Both  $\text{La}_{\text{Ce}}$  and  $\text{La}_{\text{Def}}$  display a significant increase of  $\sigma_c$  with increasing (Zr,La) content up to values as large as 20.1 MHz, evidencing a dramatic increase in structural disorder. We observe the same structural trends after annealing both these compounds at  $1200^\circ\text{C}$  (Figures 7-SI and 8-SI and Table 2-SI). The concentration of  $\text{La}_{\text{Def}}$  stays nevertheless rather constant over this range of composition.

### Raman study: introduction of a local defect model

The primitive unit-cell that drives the IR-Raman activities in a periodic network is a rhombohedron oriented along the three-fold cubic axis with cell angles equal to  $60^\circ$  to satisfy the cubic symmetry. The primitive unit cell of  $\text{CeO}_2$  contains the central Ce atom bonded to the two O atoms distributed along the rhombohedral axis which are equivalent through the center of symmetry operation  $i$  at the cation  $\text{O}_h$  site. Then, this bcc ESU (elementary structural unit) may be regarded as two imbricated (Figure 2a) perfect tetrahedra. On the basis of point group  $T_d$ , the vibrational Raman active normal mode are  $\Gamma_{\text{RAMAN}} = A_1 + E + T_2 + T'_2$ <sup>57</sup>. Therefore, the Raman active breathing mode  $F_{2g}$  of O atoms in the bcc ESU corresponds to the in-phase  $\nu_1$  symmetric stretch modes of the two perfect  $[\text{CeO}_4]^{4+}$  tetrahedra (figure 2a-b). The occurrence of an oxygen vacancy then breaks the local centrosymmetry (but also partially the translational symmetry selection rules) and the two half ESUs are no more equivalent and frequency decoupling between the imbricated  $T_d$  sites takes place and a partial release of the initial Raman selection rules occurs. Assuming a local weak dynamical distortion so that the  $T_d$  Raman activity is preserved, we have a pair of  $[\text{CeO}_4]^{4+} / [\text{Ce}\square\text{O}_3]^{2-}$  Raman bands (Fig.2a-b). In an analogous way, a cation defect breaks the local centrosymmetry and if the structural distortion of the defect ESU, related to ionic size, valence or polarizability change, is not so critical, again we expect similar Raman features. This local defect model considering two imbricated tetrahedra is the simplest molecular ESU description that can be done considering the periodic structure of ceria. We explicitly did not consider more complex situation that probably occurs but much lesser extent since the Raman spectra were sufficiently well reproduced with this simple ESU local defect model.

For the Raman spectra of  $\text{Ce}_{0.9}\text{La}_{0.1}\text{O}_{1.95}$  compounds annealed at  $600^\circ\text{C}$  and  $1200^\circ\text{C}$  (Figure 2c), the-strongest relevant difference is observed in the high frequency range ( $ca 600 \text{ cm}^{-1}$ ) associated

to  $\text{LaO}_8$  cubic site with two imbricated tetrahedral sites as proposed here. The low frequency range ( $< 250 \text{ cm}^{-1}$ ) is related to heavier cations displacements and their contributions are expected to be highly sensitive to thermal effects favoring thus potential oxygen mobility in the network. The various valence and deformation modes of  $T_d$  site, following the frequency order proposed by Nakamoto *et al.*<sup>57</sup>, are represented on Figure 9-

SI. Of course, the low frequency range decomposition that we present here is a proposition that we think consistent with the ESU local defect model. Note that this low frequency range decomposition does not impact the correlations that we evidence in this work considering the Raman high frequency range and the NMR results.

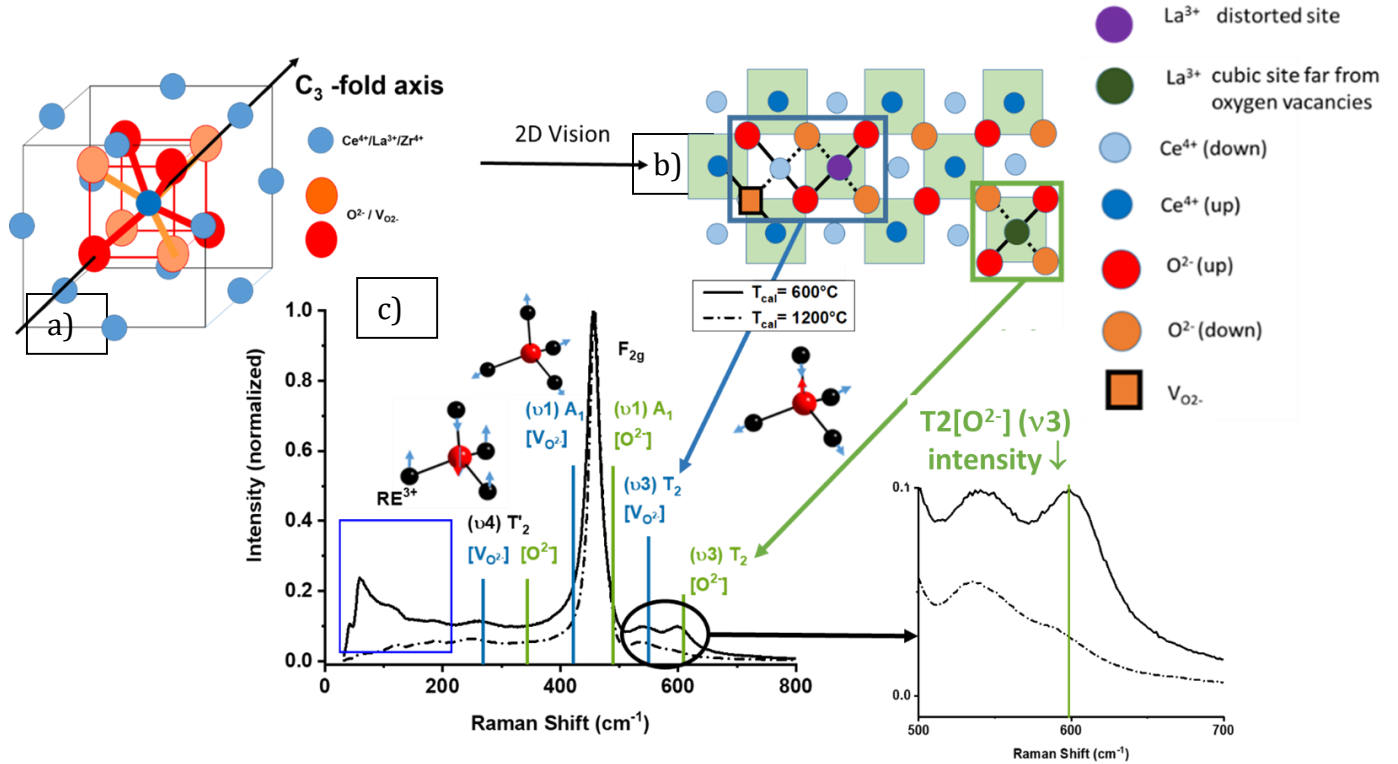


Figure 2 a) and b) Schematic representations of the ceria (fluorite) network with two imbricated oxygen tetrahedral sites surrounding cations and associated  $\text{La}^{3+}/\text{V}_{\text{O}_2-}$  defects. c) Various valence and deformation vibration modes of  $T_d$  site assigned on Raman spectra (Raman spectra of  $\text{Ce}_{0.9}\text{La}_{0.1}\text{O}_{1.95}$  annealed at  $T = 600^\circ\text{C}$  and  $T = 1200^\circ\text{C}$  appear with bold and dashed line respectively), following the frequency order proposed by Nakamoto *et al.*<sup>57</sup>.

The  $^{139}\text{La}$  NMR study evidenced that the  $\text{La}_{\text{Ce}}$  pseudo-cubic site (27 % contribution) identified for the oxide annealed at  $600^\circ\text{C}$  becomes more disordered and under the influence of  $\text{V}_{\text{O}_2-}$  upon annealing at  $1200^\circ\text{C}$ . On this basis, the high frequency band observed at  $600 \text{ cm}^{-1}$  in Raman spectra depicted in Figure 2-c, whose intensity decreases after annealing at high temperatures, should be then due to  $\text{La}_{\text{Ce}}$  sites. According to Nakamoto, this high frequency band is assigned to the asymmetric stretch  $T_2$  ( $\nu_3$ ) (Fig. 9-SI). The intensity decrease and the red-shift of this  $T_2[\text{O}^{2-}]$  band upon increasing annealing temperature (for details see in supplementary information: Fig.10a-SI and Fig. 11a-SI and Table 5-SI and Table 6-SI) can hence be related to the increased local disorder around La atoms seen by  $^{139}\text{La}$  NMR. The other band around  $550 \text{ cm}^{-1}$  at lower frequency does not change drastically (energy shift and intensity) after annealing the sample at high temperature. The  $\text{O}^{2-}\text{-La}^{3+}$  chemical bonding stiffness associated with this vibration mode is less strong than the previous one with a relaxation effect due to the occurrence of  $\text{V}_{\text{O}_2-}$  in its nearest neighborhood (Fig. 2b-c). It should correspond to an asymmetric stretch  $T_2[\text{V}_{\text{O}_2-}]$  polar mode ( $\nu_3$ ) linked

to the presence of  $\text{V}_{\text{O}_2-}$  in the nearest neighborhood of oxygen and lanthanum atoms as shown in Figure 2b. In addition to the main  $F_{2g}$  peak, six expected additional peaks between  $600 \text{ cm}^{-1}$  and  $200 \text{ cm}^{-1}$  have been indeed found. The deconvolution of Raman spectra are depicted in Fig. 10-SI and 11-SI and reported in Table 4 and Tables 4-5-6-SI. According to Nakamoto<sup>57</sup>, for a  $T_d$  site, the two bands at  $400\text{-}500 \text{ cm}^{-1}$  are attributed to the  $\nu_1$  symmetric stretch ( $A_1$ ), respectively noted  $A_1[\text{O}^{2-}]$  and  $A_1[\text{V}_{\text{O}_2-}]$ .

The  $A_1$  bands intensity decreasing for samples annealed at  $1200^\circ\text{C}$  (Figures. 2c), tend to show also that the random distribution of  $\text{V}_{\text{O}_2-}$  induces a higher (cubic) symmetry. The two last bands around  $350 \text{ cm}^{-1}$  and  $250 \text{ cm}^{-1}$ , coupled with the asymmetric stretch  $T_2$  ( $\nu_3$ ) for symmetry reasons, are assigned to the polar  $T_2$  ( $\nu_4$ ) deformation mode, also more sensitive to charge defects and respectively to  $T_d[\text{O}^{2-}]$  and  $T_d[\text{V}_{\text{O}_2-}]$  environments. The  $T_2[\text{V}_{\text{O}_2-}]$  peak around  $250 \text{ cm}^{-1}$  appears more clearly and will give complementary information. The red shift of this band and the decrease of its intensity as complex oxides are annealed

at 1200°C (Fig. 2c), seems to indicate that O atoms near  $V_{O^{2-}}$  are less bonded to  $\text{La}^{3+}/\text{Ce}^{4+}$ . That suggests the random distribution of  $V_{O^{2-}}$  into the fluorite network in good agreement with  $^{139}\text{La}$  NMR study.

In order to reasonably quantify the content of structural defects, the peak at higher energy around  $600\text{ cm}^{-1}$  and denoted  $\text{T}_2[\text{O}^{2-}]$  seems more representative because they are unambiguously separated from the other ones at lower frequencies. An intensity ratio  $N = \text{T}_2[\text{O}^{2-}] / \text{F}_{2g}$ , reported in Table 4, has been considered

for discussion involving the  $\text{T}_2[\text{O}^{2-}]$  ( $\nu_3$ ) polar mode around  $600\text{ cm}^{-1}$ , sensitive to charge defects and the main  $\text{F}_{2g}$  line. Furthermore, the Gaussian versus Lorentzian shape of the  $\text{T}_2[\text{O}^{2-}]$  peak reported in Table 4 can be also discussed.

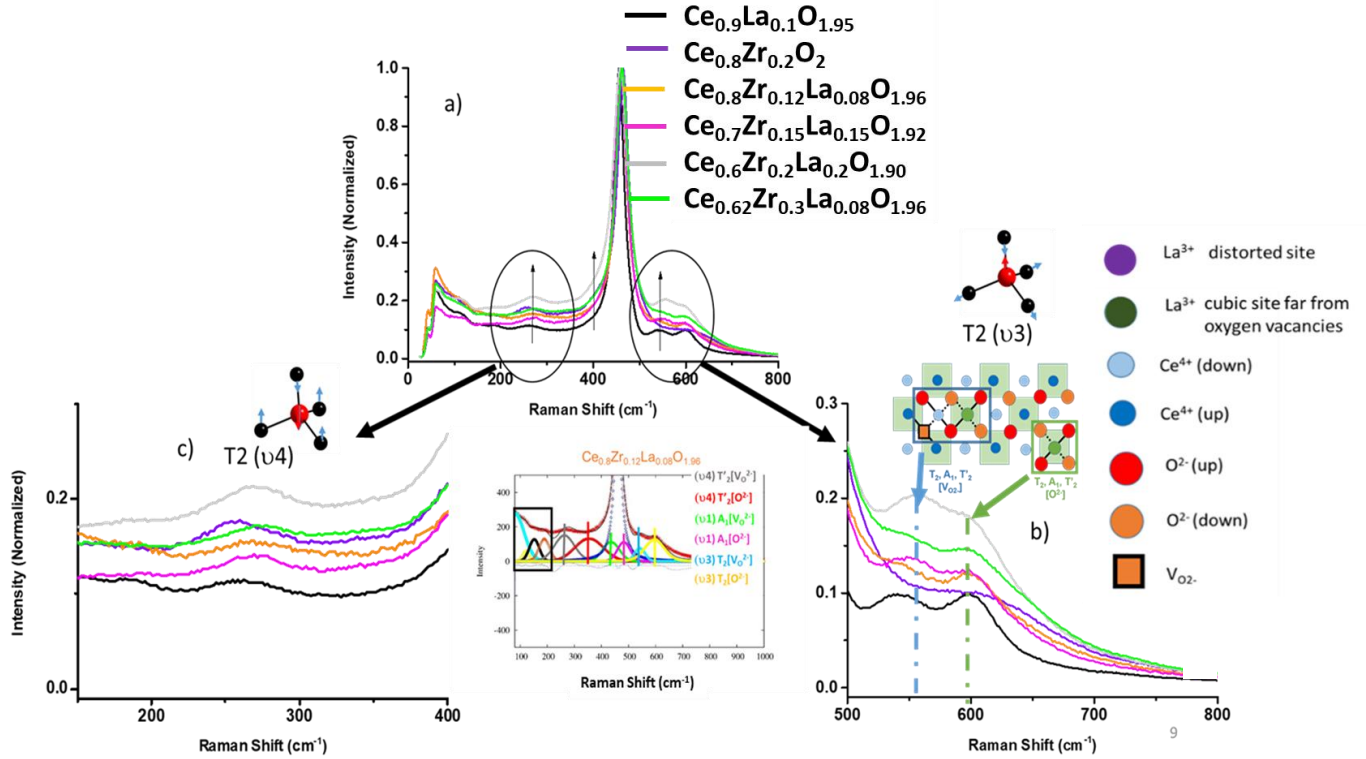


Figure 3 : Raman spectra of  $\text{Ce}_{1-x-y}\text{Zr}_x\text{RE}_y\text{O}_{2-z}$  complex oxides annealed at  $600^\circ\text{C}$  (a) with expanded view of selected region ( $500\text{--}800\text{ cm}^{-1}$ ) (b) and  $200\text{--}400\text{ cm}^{-1}$  (c) . Raman spectrum deconvolution of  $\text{Ce}_{0.8}\text{Zr}_{0.12}\text{La}_{0.08}\text{O}_{1.96}$  complex oxide annealed at  $600^\circ\text{C}$  is also represented.

When a Gaussian contribution (inhomogeneous width) to a defect band profile decreases (in favor of a Lorentzian shape: homogeneous width) it means that defects becomes more localized (i.e. less randomly distributed) and experience a longer vibrational lifetime. In other words, we think this band profile modification evidences a short range order of structural defects as well as interactions between them. Thus, the Gaussian con-

tribution equal to 50% in  $\text{Ce}_{0.9}\text{La}_{0.1}\text{O}_{1.90}$ , calcined at  $600^\circ\text{C}$  (Table 4), suggests that a new short range organization of defects is being set up. It is not the case for the  $\text{T}_2[\text{V}_{O^{2-}}]$  Raman peak with almost 100% of Gaussian shape (Table 5-SI) and for which the defects associated to oxygen vacancies remain randomly distributed.

Table 4 : Summary of the Experimental Raman Parameters extracted from spectra deconvolutions of  $Ce_{1-x-y}Zr_xRE_yO_{2-z}$  complex oxides annealed at 600°C under air

Compositions ( $T_{cal} = 600^\circ C$ )	$F_{2g}$	$T_2[O^2]$		$N$	$N_{La}$
	Intensity (a.u.)	Intensity (a.u.)	Gaussian Shape (%)	$N = \frac{T_2[O^2]}{F_{2g}}$	$N_{La} = \frac{N}{x_{La}}$
$Ce_{0.9}La_{0.1}O_{1.90}$	0.80150	0.12390	50	0.155	1.550
$Ce_{0.8}Zr_{0.12}La_{0.08}O_{1.96}$	0.37092	0.06437	65	0.174	2.175
$Ce_{0.7}Zr_{0.15}La_{0.15}O_{1.92}$	0.66590	0.15093	31	0.224	1.493
$Ce_{0.6}Zr_{0.20}La_{0.20}O_{1.90}$	0.81601	0.60329	0	0.732	3.660
$Ce_{0.62}Zr_{0.30}La_{0.08}O_{1.96}$	0.70358	0.44976	0	0.639	7.989

By analyzing the evolution of the  $T_2[O^{2-}]/F_{2g}$  intensity ratio (green arrow around  $600\text{ cm}^{-1}$  on Fig. 3c), the substitution of  $Ce^{4+}$  by  $Zr^{4+}$  in  $Ce_{0.8}Zr_{0.12}La_{0.08}O_{1.96}$  leads to the increase of the intensity ratio  $N$  in comparison with  $Ce_{0.9}La_{0.1}O_{1.90}$ , with almost the same La content (Table 4 and Fig 3). This is in agreement with the increase of the amount of  $La_{Ce}$  not influenced by  $V_{O^{2-}}$  upon increasing  $Zr^{4+}$  content, as seen by  $^{139}La$  NMR. Furthermore, the  $T_2[O^{2-}]$  peak shape exhibits a more pronounced Gaussian contribution (65%, Table 4) which suggests that structural defects are more randomly distributed in this Zr-containing compound than in  $Ce_{0.9}La_{0.1}O_{1.95}$ . Furthermore, the comparison with  $Ce_{0.8}Zr_{0.2}O_2$  spectrum, reveals clearly a flat band centered at  $600\text{ cm}^{-1}$  instead of the two  $T_2[V_{O^{2-}}]$  and  $T_2[O^{2-}]$  peaks in La-substituted cerium-based oxides (green and blue arrows on Fig. 3b). As mentioned in the literature<sup>23,30</sup>, these two Raman peaks in the high frequency region do indeed evidence the presence of trivalent rare-earth ions stabilized into the ceria-based network.

By increasing the La and  $V_{O^{2-}}$  contents in  $Ce_{0.8}Zr_{0.15}La_{0.15}O_{1.92}$  the proportion of local defects in the vicinity of La but isolated from  $V_{O^{2-}}$  slightly increases, with the intensity ratio  $N$  which varies from 0.174 in  $Ce_{0.8}Zr_{0.12}La_{0.08}O_{1.96}$  to 0.223 in  $Ce_{0.7}Zr_{0.15}La_{0.15}O_{1.92}$ . Taking into account the La content, the  $N_{La}$  value ( $N_{La} = N / x_{La}$ ) changes roughly from 2.2 for  $x = 0.08$  to 1.5 for  $x = 0.15$  (Table 4). On the basis of our  $^{139}La$  NMR investigation, the proportion of the  $La_{Ce}$  site evolves from 40% ( $Ce_{0.8}Zr_{0.12}La_{0.08}O_{1.96}$ ) to 31% ( $Ce_{0.8}Zr_{0.15}La_{0.15}O_{1.92}$ ), in good agreement with the decrease of the  $N_{La}$  value in this series. This change can be clearly observed on Figure 3b (noted by green and blue arrows) considering the  $T_2[O^{2-}]$  and  $T_2[V_{O^{2-}}]$  Raman bands.

The Gaussian contribution to the  $T_2[O^{2-}]$  peak strongly decreases to 31% (Table 4) upon increasing Zr and La content, showing that short range ordering of defects is taking place. Increasing further the Zr content leads to pure Lorentzian line shape of the  $T_2[O^{2-}]$  peak (Table 4) also pointing towards a self-organization of defects at a local scale. The frontier between the  $La_{Ce}$  pseudo-cubic site surrounded by twelve  $Ce^{4+}$  cubic sites as second neighbors and the  $La_{Def}$  local environment connected with oxygen vacancies and/or  $Zr^{4+}$  in its vicinity is then hard to distinguish using Raman data. Clusters formation involving  $V_{O^{2-}}$ , Zr, and La atoms must appear at high Zr loading, such as in  $Ce_{0.62}Zr_{0.3}La_{0.08}O_{1.96}$  for which the observed very high  $N_{La}$  value has no more sense. This is also seen in the increase of  $A_1[V_{O^{2-}}]$ ,  $T_2[V_{O^{2-}}]$  and  $T_2[V_{O^{2-}}]$  (marked with an arrow on Fig. 3a) band intensities and related to the presence of defects near  $V_{O^{2-}}$ . Moreover, the pure Lorentzian shape (homogeneous width) of the  $T_2[O^{2-}]$  peak for the oxides with the highest contents of La and Zr (Table 4) also shows the localized character of these defects (loss of connectivity with the ceria network).

For the compounds annealed at  $1200^\circ C$ , the intensity of the bands in the  $T_2(\nu_3)$  and  $T_2(\nu_4)$  region (Fig. 8-SI) drastically increases for  $Ce_{0.8}Zr_{0.2}La_{0.2}O_{1.90}$  whereas they gradually vary with La and Zr contents for the four other ones. The  $T_2[O^{2-}]$  band intensity at  $600\text{ cm}^{-1}$  increases with La content and its line shape becomes more Lorentzian, suggesting again a partial structuration of the defects at a local scale.

### ***Correlation between Raman and $^{139}La$ NMR investigations: analysis of defects.***

On the basis of  $^{139}La$  NMR study, the content of  $La_{Ce}$  pseudo-cubic sites located far from Zr and less disordered because they are less affected by oxygen vacancies than the second site  $La_{Def}$ , has been correlated to the  $N_{La}$  ratio deduced from Raman spectroscopy (Tables 3 & 4). The case of  $Ce_{0.6}Zr_{0.2}La_{0.2}O_{1.90}$  ( $T_{cal} = 600^\circ C$ ) with the highest La and Zr contents is more complex. It shows the largest  $\sigma_C$  measured by NMR for both  $La_{Ce}$  and  $La_{Def}$  environments pointing toward a severe increase in structural disorder, yet the large increase of  $T_2(\nu_3)$  band intensity at high frequency shows a partial local organization of defects. It points to specific cluster formation and it is then preferable to focus on the three  $Ce_{0.9}La_{0.1}O_{1.95}$ ,  $Ce_{0.8}Zr_{0.12}La_{0.08}O_{1.96}$  and  $Ce_{0.7}Zr_{0.15}La_{0.15}O_{1.92}$  compositions to better underline the correlations between  $^{139}La$  NMR and Raman analyses (Fig. 4-a). For those compounds, the effect of annealing temperature on the proportion of  $La_{Ce}$  pseudo-cubic sites and the  $N_{La}$  parameter has been drawn in Figure 4-b, showing a rather good correlation.

The  $La_{Ce}$  site of  $Ce_{0.9}La_{0.1}O_{1.95}$  is thermally unstable and defects disorder appears with annealing temperature. However, whatever the annealing temperature, the 50% Gaussian contribution of the Raman  $T_2[O^{2-}]$  band (Table 4) shows a partial organization of defects involving  $La_{Def}$ . The substitution of a small amount of Zr for Ce in  $Ce_{0.8}Zr_{0.12}La_{0.08}O_{1.96}$  oxide contributes to an increase in the proportion of  $La_{Ce}$  pseudo-cubic sites but also its thermal stability and the defects seem to be more randomly distributed (65% Gaussian contribution of  $T_2[O^{2-}]$  band of Raman spectrum, Table 4). Nevertheless, the increase of La and Zr contents in  $Ce_{0.7}Zr_{0.15}La_{0.15}O_{1.92}$ , does not allow the stabilization of a higher proportion of  $La_{Ce}$  sites after annealing at  $600^\circ C$  and the defects rate  $N_{La}$  associated with  $La_{Ce}$  pseudo-cubic sites also decreases with the appearance of a partial organization of such defects at a local scale (30% of Gaussian shape of  $T_2[O^{2-}]$  band of Raman spectrum, Table 4).

In the series of  $Ce_{0.9}La_{0.1}O_{1.95}$ ,  $Ce_{0.8}Zr_{0.12}La_{0.08}O_{1.96}$ , and  $Ce_{0.7}Zr_{0.15}La_{0.15}O_{1.92}$  annealed at  $1200^\circ C$ , the concentration of  $La_{Ce}$  defects far from oxygen vacancies (Raman) and the proportion of  $La_{Ce}$  pseudo-cubic sites farther from Zr atoms ( $^{139}La$  NMR) gradually increase with (La+Zr) content (Fig.4-b). Nevertheless, the local disorder also raises with high (La + Zr) content. Starting from  $Ce_{0.7}Zr_{0.15}La_{0.15}O_{1.92}$ , the local organization around

La<sup>3+</sup> and oxygen vacancies located around Zr<sup>4+</sup> looks like that observed in pyrochlore La<sub>2</sub>Zr<sub>2</sub>O<sub>7</sub> with the deformation of LaO<sub>8</sub> cubic sites near Zr<sup>4+</sup> ions. The only stable and well isolated (limitation of the local disorder with the lowest  $\sigma_C$  value related to <sup>139</sup>La NMR spectra on Table 3-SI and the highest percentage of Gaussian shape of T2[O<sup>2-</sup>] band of Raman spectra around 60% on Table 7-SI) La<sub>Ce</sub> pseudo-cubic site is observed after annealing at 1200°C for Ce<sub>0.8</sub>Zr<sub>0.12</sub>La<sub>0.08</sub>O<sub>1.96</sub> i.e. in a com-

pound with a surface area of around 10 m<sup>2</sup>/g. A schematic representation of the surface-subsurface-bulk network of the Ce<sub>0.8</sub>Zr<sub>0.12</sub>La<sub>0.08</sub>O<sub>1.96</sub> complex oxide is depicted in Figure 4c.

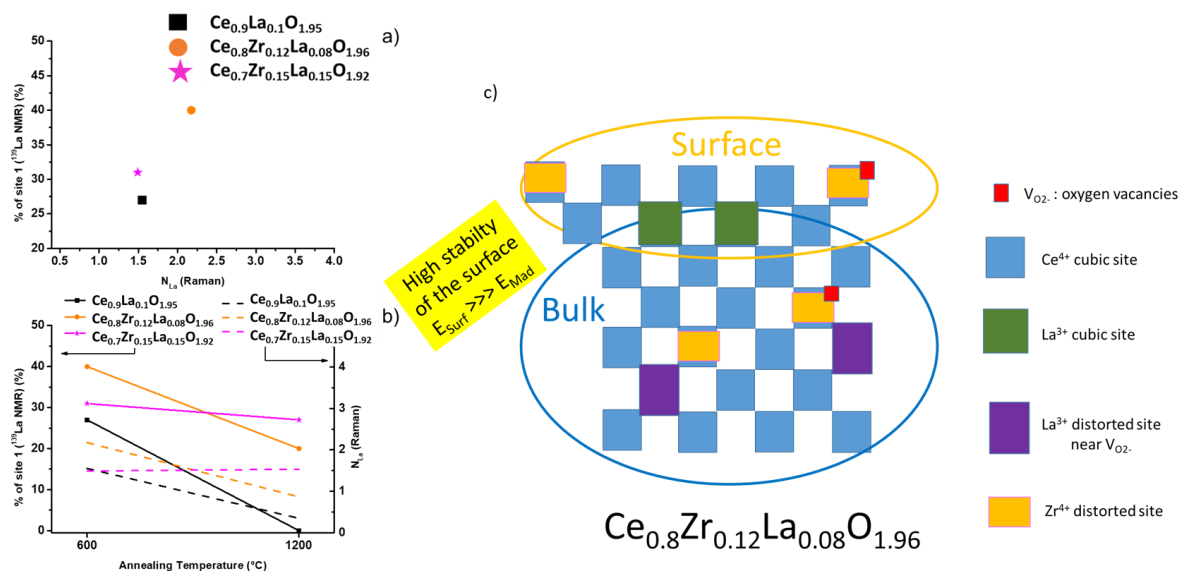


Figure 4 : Correlation between Raman and <sup>139</sup>La NMR parameters. (a): % of La<sub>Ce</sub> (pseudo-cubic site , <sup>139</sup>La NMR) versus N<sub>La</sub> (Raman) for oxides annealed at 600°C. (b): N<sub>La</sub> (Raman) and % of La<sub>Ce</sub> (<sup>139</sup>La NMR) versus annealing temperature. (c) Schematic representation of the surface-subsurface-bulk network of the Ce<sub>0.8</sub>Zr<sub>0.12</sub>La<sub>0.08</sub>O<sub>1.96</sub> oxide. La<sup>3+</sup> cubic site far from Zr<sup>4+</sup> and oxygen vacancies (La<sub>Ce</sub>) are represented in green, La<sup>3+</sup> distorted site near Zr<sup>4+</sup> and oxygen vacancies (La<sub>Def</sub>) in violet, Zr<sup>4+</sup> in orange, oxygen vacancies (V<sub>O2</sub><sup>2-</sup>) in red and Ce<sup>4+</sup> in blue.

With a small amount of Zr (12 or 15 %<sub>at</sub>), a larger content of La<sub>Ce</sub> in pseudo-cubic coordination can be stabilized and this is probably due to the large amount of isoelectronic Ce<sup>4+</sup> in the cubic site, as well as the lower interactions with smaller polarizing Zr<sup>4+</sup> cations. Moreover, this La<sub>Ce</sub> pseudo-cubic site is highly polarizable and its ability to be deformed would also promote the oxygen motion. After the oxygen displacement, La<sup>3+</sup> ions can be indeed easily stabilized with oxygen vacancies in a larger 7-fold coordinated site with higher polarizability, like in La<sub>2</sub>O<sub>3</sub> for instance. The high thermal stability of this La<sub>Ce</sub> pseudo-cubic site farther from Zr atoms, for compositions with low Zr content, seems also a key feature at the origin of sufficient surface areas after annealing at high temperatures (Table 1). This La<sub>Ce</sub> site acts as a pillar which reinforces the thermal stability of the surface (Fig.4c). The other more disordered La<sub>Def</sub> sites, whose proportion increases with the annealing temperature, is closer to oxygen vacancies and Zr atoms. Consequently, the distortion of this latter site is more pronounced in the bulk. It is then reasonable to assume that all of the more regular La<sub>Ce</sub> sites remains in the subsurface and strongly affects the oxygen

mobility at the surface. This pseudo-cubic La<sub>Ce</sub> site behaves as an oxygen pump and illustrates the strong impact of the subsurface on the oxygen availability at the surface (Fig. 4c). Nevertheless, if the surface properties are enhanced in this case, the ionic conductivity in the bulk should be lowered because of the ZrO<sub>7</sub>-LaO<sub>8</sub> clustering acting as oxygen diffusion barriers.

## CONCLUSIONS

A series of cerium-based complex oxides with increasing content of zirconium and lanthanum have been prepared by co-precipitation in basic medium followed by annealing at 600°C to keep surface area but also at 1200°C to compare the structural features of the bulk with or without the contribution of the surface. Combining <sup>139</sup>La NMR and Raman spectroscopies, allows access to information about La local environments and associated defects respectively. Two kinds of La site have been evidenced: away from Zr and consequently surrounding by Ce<sup>4+</sup> cubic site, labeled La<sub>Ce</sub> and nearby

Zr and with a higher local disorder but also the influence of oxygen vacancies in their neighborhood for the second one, labeled  $\text{La}_{\text{Def}}$ . The proportion of both these sites varies with the La and Zr contents and their local disorder becomes higher with the (La+Zr) loading. For the lowest contents (around 10%<sub>mol</sub> of La and 10%<sub>mol</sub> of Zr) the amount of  $\text{La}_{\text{Ce}}$  is the highest at around 40%. The defects detected on Raman spectra have been indexed considering tetrahedral environments around lanthanum and a pair of Raman bands with or without the influence of oxygen vacancies. It is found that for larger (La+Zr) content short range order of defects and clustering can occur. The formation of La/Zr clusters probably affects geometry of  $\text{La}_{\text{Ce}}$  site creating local distortion and disorder. The  $\text{La}_{\text{Ce}}$  pseudo-cubic site far from the oxygen vacancies for the  $\text{Ce}_{0.8}\text{Zr}_{0.12}\text{La}_{0.08}\text{O}_{1.96}$  composition containing the lowest La and Zr contents, is the most isolated one in this series. Thus, the isolated  $\text{LaO}_8$  defect detected at high frequency on Raman spectra can be correlated to the  $\text{La}_{\text{Ce}}$  pseudo-cubic site, farther from Zr and oxygen vacancies and observed in  $^{139}\text{La}$  NMR spectra. This is the first time that a new indexing of Raman bands associated with defects in ceria-based materials is proposed based on an  $^{139}\text{La}$  NMR study, so illustrating the interconnections between the oxygen and cationic sub-networks. When the La and Zr contents are low around 10%<sub>at</sub> in order to limit the interactions between them, the percentage of isolated  $\text{La}_{\text{Ce}}$  pseudo-cubic site connected to the oxygen  $\text{T}_d$  site far from oxygen vacancies is the highest. The strong ionic character of the La-O bonding in this cubic site should lead to enhanced the oxygen mobility at the surface. This structural defect behaves as an oxygen pump at the subsurface to feed the oxygen vacancies surrounding few  $\text{Zr}^{4+}$  ions at the surface. Moreover, the larger the  $\text{La}_{\text{Ce}}$  concentration (more disordered as the (La+Zr) content increases), the higher the thermal stability in order to keep high surface area at high temperatures. This  $\text{La}_{\text{Ce}}$  pseudo-cubic site far from Zr atoms contributes to increase the surface energy to the detriment of the Madelung energy which tends to associate the most polarizable rare earth  $\text{La}^{3+}$  to the most polarizing cation,  $\text{Zr}^{4+}$ .

This study opens up the field of new structures and heterostructures with defined compositions aimed at increasing oxygen mobility while maintaining a high specific surface area. One of the challenges will be to finely modify the composition of  $\text{Ce}_{0.5}\text{Zr}_{0.5}\text{O}_2$  mixed oxide which exhibit excellent OSC properties in order to increase both the oxygen mobility and thermal stability. As mentioned in this paper, the local environment of  $\text{La}^{3+}$  can be strongly influenced by the smaller ions  $\text{Zr}^{4+}$  or more polarizing  $\text{Nb}^{5+}$ . Finally, the cubic environment of La as in  $\text{LaNbO}_4$  can be an interesting starting point in order to identify new compositions and structures where oxygen mobility would be enhanced for applications in redox catalysis and Solid Oxide Fuel Cells.

## ASSOCIATED CONTENT

### Supporting Information.

Figure S1 showing powder XRD patterns of  $\text{Ce}_{1-x-y}\text{Zr}_x\text{RE}_y\text{O}_{2-z}$  complex oxides annealed at 600°C under air. Figure S2 showing powder XRD patterns of  $\text{Ce}_{1-x-y}\text{Zr}_x\text{RE}_y\text{O}_{2-z}$  complex oxides annealed at 1200°C under air. Figure S3 showing the comparison of the best fit simulations of the  $^{139}\text{La}$  NMR spectra of  $\text{Ce}_{0.9}\text{La}_{0.1}\text{O}_{1.95}$  annealed at 600°C and using one- (left) and two- (right) Czjzek-like components. Simulations account simultaneously for the static (top) and spinning (bottom) experimental spectra. Figure S4 showing the comparison of the best fit simulations of the  $^{139}\text{La}$  NMR spectra of  $\text{Ce}_{0.8}\text{Zr}_{0.12}\text{La}_{0.08}\text{O}_{1.96}$  annealed at 600°C and using one- (left) and two- (right) Czjzek-like components. Simulations account simultaneously for the static (top) and spinning (bottom) experimental spectra. Figure S5 showing the comparison of the best fit simulations of the  $^{139}\text{La}$  NMR spectra of  $\text{Ce}_{0.9}\text{La}_{0.1}\text{O}_{1.95}$  annealed at 1200°C and using one- (left) and two- (right) Czjzek-like components. Simulations account simultaneously for the static (top) and spinning (bottom) experimental spectra. Figure S6 showing the comparison of the best fit simulations of the  $^{139}\text{La}$  NMR spectra of  $\text{Ce}_{0.84}\text{Zr}_{0.12}\text{La}_{0.08}\text{O}_{1.96}$  annealed at 1200°C and using one- (left) and two- (right) Czjzek-like components. Simulations account simultaneously for the static (top) and spinning (bottom) experimental spectra. Figure S7 showing the best fit simulations of the  $^{139}\text{La}$  NMR spectra of  $\text{Ce}_{0.70}\text{Zr}_{0.15}\text{La}_{0.15}\text{O}_{1.95}$  annealed at 600°C (left) and 1200°C (right) and using two Czjzek-like components. Simulations account simultaneously for the static (top) and spinning (bottom) experimental spectra. Figure S8 showing the best fit simulations of the  $^{139}\text{La}$  NMR spectra of  $\text{Ce}_{0.60}\text{Zr}_{0.20}\text{La}_{0.20}\text{O}_{1.90}$  annealed at 600°C (left) and 1200°C (right) and using two Czjzek-like components. Simulations account simultaneously for the static (top) and spinning (bottom) experimental spectra. Figure S9 showing the schematic representation of various valence and deformation vibration mode of  $\text{T}_d$  site, following the frequency order proposed by Nakamoto. Figure S10 showing the Raman spectra deconvolution of  $\text{Ce}_{1-x-y}\text{Zr}_x\text{La}_y\text{O}_{2-z}$  complex oxides annealed at 600°C. Figure S11 showing the Raman spectra deconvolution of  $\text{Ce}_{1-x-y}\text{Zr}_x\text{La}_y\text{O}_{2-z}$  complex oxides annealed at 1200°C. Figure S12 showing the Raman spectra of  $\text{Ce}_{1-x-y}\text{Zr}_x\text{La}_y\text{O}_{2-z}$  complex oxides annealed at 1200°C. Table S1 showing the ICP analysis of complex oxides. Table S2 showing Structural and textural characteristics of  $\text{Ce}_{1-x-y}\text{Zr}_x\text{RE}_y\text{O}_{2-z}$  oxides annealed at 1200°C under air. Table S3 showing Experimental  $^{139}\text{La}$  NMR Parameters of  $\text{Ce}_{1-x-y}\text{Zr}_x\text{RE}_y\text{O}_{2-z}$  complex oxides annealed at 1200°C under air. Table S4 showing experimental  $^{139}\text{La}$  NMR Parameters of  $\text{Ce}_{1-x-y}\text{Zr}_x\text{RE}_y\text{O}_{2-z}$  complex oxides with error bars. Table S5 showing Supplementary Experimental RAMAN Parameters extracted from spectra deconvolutions of  $\text{Ce}_{1-x-y}\text{Zr}_x\text{RE}_y\text{O}_{2-z}$  complex oxides annealed at 1200°C under air. Table S6 Experimental RAMAN Parameters extracted from spectra deconvolutions of  $\text{Ce}_{1-x-y}\text{Zr}_x\text{RE}_y\text{O}_{2-z}$  complex oxides annealed at 1200°C under air. Table S7 showing Supplementary Experimental RAMAN Parameters extracted from spectra deconvolutions of  $\text{Ce}_{1-x-y}\text{Zr}_x\text{RE}_y\text{O}_{2-z}$  complex oxides annealed at 1200°C under air.

## AUTHOR INFORMATION

### Corresponding Author

\* Alain Demourgues

[alain.demourgues@icmcb.cnrs.fr](mailto:alain.demourgues@icmcb.cnrs.fr)

### Author Contributions

The manuscript was written through contributions of all authors. / All authors have given approval to the final version of the manuscript.

## ACKNOWLEDGMENT

The authors would like to thank the French National Research Agency for the financial support (ANR, Coral Project, ref. ANR-17-CE08-0022-03)

This work has been partly done in the frame of “the Investments for the future” Programme IdEx Bordeaux – LAPHIA (ANR-10-IDEX-03-02). V.R. is grateful to the CNRS and Région Nouvelle Aquitaine for funding support.

## REFERENCES

- (1) Vidmar, P.; Fornasiero, P.; Kašpar, J.; Gubitosa, G.; Graziani, M. Effects of Trivalent Dopants on the Redox Properties of Ce<sub>0.6</sub>Zr<sub>0.4</sub>O<sub>2</sub> Mixed Oxide. *J. Catal.* **1997**, *171* (1), 160–168. <https://doi.org/10.1006/JCAT.1997.1784>.
- (2) Prasad, D. H.; Park, S. Y.; Ji, H. I.; Kim, H. R.; Son, J. W.; Kim, B. K.; Lee, H. W.; Lee, J. H. Structural Characterization and Catalytic Activity of Ce<sub>0.65</sub>Zr<sub>0.25</sub>RE<sub>0.10</sub>2- $\delta$  Nanocrystalline Powders Synthesized by the Glycine-Nitrate Process. *J. Phys. Chem. C* **2012**, *116* (5), 3467–3476. <https://doi.org/10.1021/jp207107j>.
- (3) White, W. B. *Handbook on the Physics and Chemistry of Rare Earths, Volume 13*; 1991; Vol. 26. [https://doi.org/10.1016/0025-5408\(91\)90133-7](https://doi.org/10.1016/0025-5408(91)90133-7).
- (4) Ikryannikova, L. N.; Aksenov, A. A.; Markaryan, G. L.; Murav'eva, G. P.; Kostyuk, B. G.; Kharlanov, A. N.; Lunina, E. V. Red-Ox Treatments Influence on the Structure and Properties of M<sub>2</sub>O<sub>3</sub>-CeO<sub>2</sub>-ZrO<sub>2</sub> (M = Y, La) Solid Solutions. *Appl. Catal. A Gen.* **2001**, *210* (1–2), 225–235. [https://doi.org/10.1016/S0926-860X\(00\)00811-5](https://doi.org/10.1016/S0926-860X(00)00811-5).
- (5) Kašpar, J.; Fornasiero, P.; Graziani, M. Use of CeO<sub>2</sub>-Based Oxides in the Three-Way Catalysis. *Catal. Today* **1999**, *50* (2), 285–298. [https://doi.org/10.1016/S0920-5861\(98\)00510-0](https://doi.org/10.1016/S0920-5861(98)00510-0).
- (6) Montini, T.; Melchionna, M.; Monai, M.; Fornasiero, P. Fundamentals and Catalytic Applications of CeO<sub>2</sub>-Based Materials. *Chem. Rev.* **2016**, *116* (10), 5987–6041. <https://doi.org/10.1021/acs.chemrev.5b00603>.
- (7) Yashima, M. Invited Review: Some Recent Developments in the Atomic-Scale Characterization of Structural and Transport Properties of Ceria-Based Catalysts and Ionic Conductors. *Catal. Today* **2015**, *253*, 3–19. <https://doi.org/10.1016/j.cattod.2015.03.034>.
- (8) Kharton, V. V.; Figueiredo, F. M.; Navarro, L.; Naumovich, E. N.; Kovalevsky, A. V.; Yaremchenko, A. A.; Viskup, A. P.; Carneiro, A.; Marques, F. M. B.; Frade, J. R. Ceria-Based Materials for Solid Oxide Fuel Cells. *J. Mater. Sci.* **2001**, *36* (5), 1105–1117. <https://doi.org/10.1023/A:1004817506146>.
- (9) He, H.; Dai, H. X.; Wong, K. W.; Au, C. T. RE<sub>0.6</sub>Zr<sub>0.4</sub>-XY<sub>x</sub>O<sub>2</sub> (RE = Ce, Pr; X = O, 0.05) Solid Solutions: An Investigation on Defective Structure, Oxygen Mobility, Oxygen Storage Capacity, and Redox Properties. *Appl. Catal. A Gen.* **2003**, *251* (1), 61–74. [https://doi.org/10.1016/S0926-860X\(03\)00309-0](https://doi.org/10.1016/S0926-860X(03)00309-0).
- (10) Yao, H. C.; Yao, Y. F. Y. Ceria in Automotive Exhaust Catalysts. I. Oxygen Storage. *J. Catal.* **1984**, *86* (2), 254–265. [https://doi.org/10.1016/0021-9517\(84\)90371-3](https://doi.org/10.1016/0021-9517(84)90371-3).
- (11) Madier, Y.; Descorme, C.; Le Govic, A. M.; Duprez, D. Oxygen Mobility in CeO<sub>2</sub> and CexZr(1-x)O<sub>2</sub> Compounds: Study by CO Transient Oxidation And 18O/16O Isotopic Exchange. *J. Phys. Chem. B* **1999**, *103* (50), 10999–11006. <https://doi.org/10.1021/jp991270a>.
- (12) Yang, Z.; Woo, T. K.; Hermansson, K. Effects of Zr Doping on Stoichiometric and Reduced Ceria: A First-Principles Study. *J. Chem. Phys.* **2006**, *124*, 224704. <https://doi.org/10.1063/1.2200354>.
- (13) Wang, H. F.; Guo, Y. L.; Lu, G. Z.; Hu, P. Maximizing the Localized Relaxation: The Origin of the Outstanding Oxygen Storage Capacity of  $\kappa$ -Ce<sub>2</sub>Zr<sub>2</sub>O<sub>8</sub>. *Angew. Chemie - Int. Ed.* **2009**, *48* (44), 8289–8292. <https://doi.org/10.1002/anie.200903907>.
- (14) Rührup, V.; Wiemhöfer, H.-D. Ionic Conductivity of Gd- and Y-Doped Ceria-Zirconia Solid Solutions. *Zeitschrift für Naturforsch. B* **2006**, *61* (7), 916–922. <https://doi.org/10.1515/ZNB-2006-0721>.
- (15) Mori, T.; Drennan, J.; Lee, J. H.; Li, J. G.; Ikegami, T. Oxide Ionic Conductivity and Microstructures of Sm- or La-Doped CeO<sub>2</sub>-Based Systems. *Solid State Ionics* **2002**, *154–155*, 461–466. <https://doi.org/10.1016/S0167->

- 2738(02)00483-6.
- (16) Sha, X.; Lü, Z.; Huang, X.; Miao, J.; Ding, Z.; Xin, X.; Su, W. Study on La and Y Co-Doped Ceria-Based Electrolyte Materials. *J. Alloys Compd.* **2007**, *428* (1–2), 59–64. <https://doi.org/10.1016/j.jallcom.2006.03.077>.
- (17) Rohart, E.; Verdier, S.; Demourgues, A.; Harlé, V.; Pacaud, B.; Baylet, A.; Takemori, H.; Suda, E.; Allain, M. New CeO<sub>2</sub>-ZrO<sub>2</sub> Mixed Oxides with Improved Redox Properties for Advanced TWC Catalysts. *SAE Tech. Pap.* **2006**, *2006-01-0852*. <https://doi.org/10.4271/2006-01-0852>.
- (18) Wang, Q.; Zhao, B.; Li, G.; Zhou, R. Application of Rare Earth Modified Zr-Based Ceria-Zirconia Solid Solution in Three-Way Catalyst for Automotive Emission Control. *Environ. Sci. Technol.* **2010**, *44* (10), 3870–3875. <https://doi.org/10.1021/es903957e>.
- (19) Pijolat, M.; Prin, M.; Soustelle, M.; Touret, O.; Nortier, P. Thermal Stability of Doped Ceria: Experiment and Modelling. *J. Chem. Soc. Faraday Trans.* **1995**, *91* (21), 3941–3948. <https://doi.org/10.1039/FT9959103941>.
- (20) Malavasi, L.; Fisher, C. A. J.; Islam, M. S. Oxide-Ion and Proton Conducting Electrolyte Materials for Clean Energy Applications: Structural and Mechanistic Features. *Chem. Soc. Rev.* **2010**, *39* (11), 4370–4387. <https://doi.org/10.1039/b915141a>.
- (21) Mochizuki, S. Infrared Optical Properties of Cerium Dioxide. *Phys. status solidi* **1982**, *114* (1), 189–199. <https://doi.org/10.1002/PSSB.2221140122>.
- (22) Shimanouchi, T.; Tsuboi, M.; Miyazawa, T. Optically Active Lattice Vibrations as Treated by the GF-Matrix Method. *J. Chem. Phys.* **2004**, *35* (5), 1597. <https://doi.org/10.1063/1.1732116>.
- (23) Nakajima, A.; Yoshihara, A.; Ishigame, M. Defect-Induced Raman Spectra in Doped CeO<sub>2</sub>. *Phys. Rev. B* **1994**, *50* (18), 13297–13307. <https://doi.org/10.1103/PhysRevB.50.13297>.
- (24) McBride, J. R.; Hass, K. C.; Poindexter, B. D.; Weber, W. H. Raman and X-Ray Studies of Ce<sub>1-x</sub>RE<sub>x</sub>O<sub>2-y</sub>, Where RE=La, Pr, Nd, Eu, Gd, and Tb. *J. Appl. Phys.* **1994**, *76* (4), 2435–2441. <https://doi.org/10.1063/1.357593>.
- (25) He, D.; Chen, D.; Hao, H.; Yu, J.; Liu, J.; Lu, J.; Liu, F.; Wan, G.; He, S.; Luo, Y. Structural/Surface Characterization and Catalytic Evaluation of Rare-Earth (Y, Sm and La) Doped Ceria Composite Oxides for CH<sub>3</sub>SH Catalytic Decomposition. *Appl. Surf. Sci.* **2016**, *390*, 959–967. <https://doi.org/10.1016/j.apsusc.2016.08.129>.
- (26) Li, L.; Chen, F.; Lu, J. Q.; Luo, M. F. Study of Defect Sites in Ce<sub>1-x</sub>M<sub>x</sub>O<sub>2-δ</sub> (x = 0.2) Solid Solutions Using Raman Spectroscopy. *J. Phys. Chem. A* **2011**, *115* (27), 7972–7977. <https://doi.org/10.1021/jp203921m>.
- (27) Acharya, S. A.; Gaikwad, V. M.; D'Souza, S. W.; Barman, S. R. Gd/Sm Dopant-Modified Oxidation State and Defect Generation in Nano-Ceria. *Solid State Ionics* **2014**, *260*, 21–29. <https://doi.org/10.1016/j.ssi.2014.03.008>.
- (28) Acharya, S. A.; Gaikwad, V. M.; Sathe, V.; Kulkarni, S. K. Influence of Gadolinium Doping on the Structure and Defects of Ceria under Fuel Cell Operating Temperature. *Appl. Phys. Lett.* **2014**, *104* (11), 0–5. <https://doi.org/10.1063/1.4869116>.
- (29) Coduri, M.; Scavini, M.; Pani, M.; Carnasciali, M. M.; Klein, H.; Artini, C. From Nano to Microcrystals: Effects of Different Synthetic Pathways on the Defect Architecture in Heavily Gd-Doped Ceria. *Phys. Chem. Chem. Phys.* **2017**, *19* (18), 11612–11630. <https://doi.org/10.1039/c6cp08173h>.
- (30) Artini, C.; Carnasciali, M. M.; Plaisier, J. R.; Costa, G. A.; Pani, M. A Novel Method for the Evaluation of the Rare Earth (RE) Coordination Number in RE-Doped Ceria through Raman Spectroscopy. *Solid State Ionics* **2017**, *311* (September), 90–97. <https://doi.org/10.1016/j.ssi.2017.09.016>.
- (31) Devaiah, D.; Tsuzuki, T.; Aniz, C. U.; Reddy, B. M. Enhanced CO and Soot Oxidation Activity over Y-Doped Ceria-Zirconia and Ceria-Lanthana Solid Solutions. *Catal. Letters* **2015**, *145* (5), 1206–1216. <https://doi.org/10.1007/s10562-015-1507-6>.
- (32) Andriopoulou, C.; Trimpalis, A.; Petalidou, K. C.; Sgoura, A.; Efstathiou, A. M.; Boghosian, S. Structural and Redox Properties of Ce<sub>1-x</sub>Zr<sub>x</sub>O<sub>2-δ</sub> and Ce<sub>0.8</sub>Zr<sub>0.15</sub>RE<sub>0.05</sub>O<sub>2-δ</sub> (RE: La, Nd, Pr, Y) Solids Studied by High Temperature in Situ Raman Spectroscopy. *J. Phys. Chem. C* **2017**, *121* (14), 7931–7943. <https://doi.org/10.1021/acs.jpcc.7b00515>.
- (33) Harshini, D.; Lee, D. H.; Jeong, J.; Kim, Y.; Nam, S. W.; Ham, H. C.; Han, J. H.; Lim, T. H.; Yoon, C. W. Enhanced Oxygen Storage Capacity of Ce<sub>0.65</sub>Hf<sub>0.25</sub>M<sub>0.10</sub>O<sub>2-δ</sub> (M=rare Earth Elements): Applications to Methane Steam Reforming with High

- Coking Resistance. *Appl. Catal. B Environ.* **2014**, *148–149*, 415–423. <https://doi.org/10.1016/j.apcatb.2013.11.022>.
- (34) Taniguchi, T.; Watanabe, T.; Sugiyama, N.; Subramani, A. K.; Wagata, H.; Matsushita, N.; Yoshimura, M. Identifying Defects in Ceria-Based Nanocrystals by UV Resonance Raman Spectroscopy. *J. Phys. Chem. C* **2009**, *113* (46), 19789–19793. <https://doi.org/10.1021/jp9049457>.
- (35) Maekawa, H.; Kawata, K.; Xiong, Y. P.; Sakai, N.; Yokokawa, H. Quantification of Local Oxygen Defects around Yttrium Ions for Ytria-Doped Ceria-Zirconia Ternary System. *Solid State Ionics* **2009**, *180* (4–5), 314–319. <https://doi.org/10.1016/j.ssi.2009.01.015>.
- (36) Avila-Paredes, H. J.; Shvareva, T.; Chen, W.; Navrotsky, A.; Kim, S. A Correlation between the Ionic Conductivities and the Formation Enthalpies of Trivalent-Doped Ceria at Relatively Low Temperatures. *Phys. Chem. Chem. Phys.* **2009**, *11* (38), 8580–8585. <https://doi.org/10.1039/B821982F>.
- (37) Deguchi, H.; Yoshida, H.; Inagaki, T.; Horiuchi, M. EXAFS Study of Doped Ceria Using Multiple Data Set Fit. *Solid State Ionics* **2005**, *176* (23–24), 1817–1825. <https://doi.org/10.1016/j.ssi.2005.04.043>.
- (38) Scavini, M.; Coduri, M.; Allieta, M.; Brunelli, M.; Ferrero, C. Probing Complex Disorder in Ce<sub>1-x</sub>Gd<sub>x</sub>O<sub>2-x/2</sub> Using the Pair Distribution Function Analysis. *Chem. Mater.* **2012**, *24* (7), 1338–1345. <https://doi.org/10.1021/CM203819U>.
- (39) Coduri, M.; Scavini, M.; Brunelli, M.; Masala, P. In Situ Pair Distribution Function Study on Lanthanum Doped Ceria. *Phys. Chem. Chem. Phys.* **2013**, *15* (22), 8495–8505. <https://doi.org/10.1039/C3CP44300K>.
- (40) and, N. K.; Stebbins, J. F. Vacancy and Cation Distribution in Ytria-Doped Ceria: An 89Y and 17O MAS NMR Study. *Chem. Mater.* **2007**, *19* (23), 5742–5747. <https://doi.org/10.1021/CM0715388>.
- (41) Tolla, B.; Demourgues, A.; Isnard, O.; Menetrier, M.; Pouchard, M.; Rabardel, L.; Seguelong, T. Structural Investigation of Oxygen Insertion within the Ce<sub>2</sub>Sn<sub>2</sub>O<sub>7</sub>–Ce<sub>2</sub>Sn<sub>2</sub>O<sub>8</sub> Pyrochlore Solid Solution by Means of in Situ Neutron Diffraction Experiments. *J. Mater. Chem.* **1999**, *9* (12), 3131–3136. <https://doi.org/10.1039/A905914H>.
- (42) Moog, I.; Prestipino, C.; Figueroa, S.; Majimel, J.; Demourgues, A. Dual Ce<sup>4+</sup>/Fe<sup>3+</sup> Redox Phenomena into Nanocrystalline Ce<sub>1-x</sub>Fe<sub>x</sub>O<sub>2-x/2</sub> Solid Solution. *J. Phys. Chem. C* **2014**, *118* (39), 22746–22753. <https://doi.org/10.1021/JP505224V>.
- (43) Moog, I.; Feral-Martin, C.; Duttine, M.; Wattiaux, A.; Prestipino, C.; Figueroa, S.; Majimel, J.; Demourgues, A. Local Organization of Fe<sup>3+</sup> into Nano-CeO<sub>2</sub> with Controlled Morphologies and Its Impact on Reducibility Properties. *J. Mater. Chem. A* **2014**, *2* (47), 20402–20414. <https://doi.org/10.1039/C4TA02631D>.
- (44) Frizon, V.; Bassat, J. M.; Pollet, M.; Durand, E.; Hernandez, J.; Pajot, K.; Vernoux, P.; Demourgues, A. Tuning the Pr Valence State to Design High Oxygen Mobility, Redox and Transport Properties in the CeO<sub>2</sub>-ZrO<sub>2</sub>-PrO<sub>x</sub> Phase Diagram. *J. Phys. Chem. C* **2019**, *123* (11), 6351–6362. <https://doi.org/10.1021/ACS.JPCC.8B11469>.
- (45) Tabira, Y.; Withers, R. L.; Yamada, T.; Ishizawa, N. Annular Dynamical Disorder of the Rare Earth Ions in a La<sub>2</sub>Zr<sub>2</sub>O<sub>7</sub> Pyrochlore via Single Crystal Synchrotron X-Ray Diffraction. *Zeitschrift fur Krist.* **2001**, *216* (2), 92–98. <https://doi.org/10.1524/zkri.216.2.92.20338>.
- (46) Czjzek, G.; Fink, J.; Götz, F.; Schmidt, H.; Coey, J. M. D.; Rebouillat, J. P.; Liénard, A. Atomic Coordination and the Distribution of Electric Field Gradients in Amorphous Solids. *Phys. Rev. B* **1981**, *23* (6), 2513–2530. <https://doi.org/10.1103/PhysRevB.23.2513>.
- (47) d’Espinoze de Lacaillerie, J. B.; Fretigny, C.; Massiot, D. MAS NMR Spectra of Quadrupolar Nuclei in Disordered Solids: The Czjzek Model. *J. Magn. Reson.* **2008**, *192* (2), 244–251. <https://doi.org/10.1016/J.JMR.2008.03.001>.
- (48) Massiot, D.; Fayon, F.; Capron, M.; King, I.; Le Calvé, S.; Alonso, B.; Durand, J. O.; Bujoli, B.; Gan, Z.; Hoatson, G. Modelling One- and Two-Dimensional Solid-State NMR Spectra. *Magn. Reson. Chem.* **2002**, *40* (1), 70–76. <https://doi.org/10.1002/mrc.984>.
- (49) Dupree, R.; Lewis, M. H.; Smith, M. E. A High-Resolution NMR Study of the La-Si-Al-O-N System. *J. Am. Chem. Soc.* **1989**, *111* (14), 5125–5132. <https://doi.org/10.1021/ja00196a016>.
- (50) Dithmer, L.; Lipton, A. S.; Reitzel, K.; Warner, T. E.; Lundberg, D.; Nielsen, U. G. Characterization of Phosphate Sequestration by a Lanthanum Modified Bentonite Clay: A Solid-State NMR, EXAFS, and PXRD

- Study. *Environ. Sci. Technol.* **2015**, *49* (7), 4559–4566.  
<https://doi.org/10.1021/es506182s>.
- (51) O'Neill, W. M.; Morris, M. A. The Defect Chemistry of Lanthana-Ceria Mixed Oxides by MASNMR. *Chem. Phys. Lett.* **1999**, *305* (5–6), 389–394.  
[https://doi.org/10.1016/S0009-2614\(99\)00343-7](https://doi.org/10.1016/S0009-2614(99)00343-7).
- (52) Paterson, A. L.; Hanson, M. A.; Werner-Zwanziger, U.; Zwanziger, J. W. Relating <sup>139</sup>La Quadrupolar Coupling Constants to Polyhedral Distortion in Crystalline Structures. *J. Phys. Chem. C* **2015**, *119* (45), 25508–25517.  
<https://doi.org/10.1021/acs.jpcc.5b09122>.
- (53) Spencer, L.; Coomes, E.; Ye, E.; Terskikh, V.; Ramzy, A.; Thangadurai, V.; Goward, G. R. Structural Analysis of Lanthanum-Containing Battery Materials Using <sup>139</sup>La Solid-State NMR. *Can. J. Chem.* **2011**, *89* (9), 1105–1117.  
<https://doi.org/10.1139/v11-049>.
- (54) Caër, G. Le; Brand, R. A. General Models for the Distributions of Electric Field Gradients in Disordered Solids. *J. Phys. Condens. Matter* **1998**, *10* (47), 10715.  
<https://doi.org/10.1088/0953-8984/10/47/020>.
- (55) Stöckmann, H. A. Electric Field Gradients Resulting from Randomly Distributed Unscreened Point Charges. *J. Magn. Reson.* **1981**, *44* (1), 145–158.  
[https://doi.org/10.1016/0022-2364\(81\)90198-0](https://doi.org/10.1016/0022-2364(81)90198-0).
- (56) Lacaillerie, J. de; Fretigny, C.; Resonance, D. M.-J. of M.; 2008, undefined. MAS NMR Spectra of Quadrupolar Nuclei in Disordered Solids: The Czjzek Model. *Elsevier*.
- (57) Nakamoto, K. *Infrared and Raman Spectra of Inorganic and Coordination Compounds: Part B: Applications in Coordination, Organometallic, and Bioinorganic Chemistry*; 2008. Wiley Ed.  
<https://doi.org/10.1002/9780470405888>.